Quantifying photodegradation of peatland-derived dissolved organic carbon in the coastal ocean of Southeast Asia

Yongli Zhou[1,*, †], Moritz Müller[2], Nagur Cherukuru[3], Patrick Martin[1,*]

[1]Asian School of the Environment, Nanyang Technological University, 639798 Singapore

[2]Faculty of Engineering, Computing and Science, Swinburne University of Science and Technology, 93350 Kuching, Sarawak, Malaysia

[3]CSIRO Oceans and Atmosphere Flagship, Canberra ACT 2601, Australia

[†]Current address: the Ecosystems Center, Marine Biological Laboratory, Woods Hole, 02543, United States

Email:

Yongli Zhou*: zhou0303@e.ntu.edu.sg

Moritz Müller: mmueller@swinburne.edu.my

Nagur Cherukuru: Nagur.Cherukuru@csiro.au

Patrick Martin*: pmartin@ntu.edu.sg

*Corresponding author(s)

Abstract

The terrigenous dissolved organic carbon (tDOC) exported from the peatlands in Southeast Asia appears to be extensively remineralized in the shelf sea, but the processes that drive this remineralization remain unclear. Here, we combined incubation experiments and model simulations to quantify the rate and extent of photodegradation of tDOC in the Sunda Shelf Sea. Laboratory photodegradation experiments indicate that up to 74% of the peatland tDOC is potentially labile to photochemical remineralization. Based on our estimated apparent quantum yield for tDOC remineralization, modeled *in-situ* solar irradiance, and measured inherent optical properties of the water column, we simulated peatland tDOC photoremineralization for two coastal regions of the Sunda Shelf Sea. These simulation results show that natural solar radiation can directly remineralize 20±11% of tDOC over 2 years, which corresponds to the approximate residence time of water in the Sunda Shelf Sea, and that significant photobleaching of tDOC can occur in coastal waters over shorter time-scales. We further derived a simplified photochemical decay constant $\emptyset^{ref}$ of 0.008–0.017day^{-1} for Southeast Asia's peatland-derived tDOC, which can be used to parameterize the recently proposed UniDOM model framework. We conclude that direct photodegradation may be a greater sink for tDOC in Southeast Asia's coastal ocean compared to higher latitudes, although it is insufficient to account for the total tDOC remineralization observed in the Sunda Shelf Sea.

Plain Language Summary

Tropical peatlands in Southeast Asia are contributing large quantity of organic carbon to the coastal ocean. This organic carbon flux is rapidly decomposed to CO_2 but the mechanism of this extensive remineralization is unclear. Organic carbon from peatlands appears to be easily decomposed upon exposure to sunlight, known as photodegradation. In this study, we conducted incubation experiments to collect data of photochemical decay efficiency of peatland-derived organic carbon and developed model simulation to calculate, in natural coastal waters, how much of the organic carbon is decomposed via the pathway of photodegradation. Our data show that sunlight radiation can directly cause a loss of 20% of the peatland-derived organic carbon input in the coastal ocean of Southeast Asia, indicating that photodegradation contribute to a larger portion of the total organic carbon decomposition in Southeast Asia than in coastal oceans at the higher latitudes. In addition, our data allowed us to derive region-specific decay rates of photodegradation for coastal ocean of Southeast Asia, which can be used to parameterize large-scale aquatic organic carbon biogeochemistry model.

1 Introduction

The biogeochemical fate of terrigenous dissolved organic carbon (tDOC) in the ocean is still poorly understood. This is important in the context of the global carbon cycle, because the riverine input and the biogeochemical processing of tDOC can have significant impacts on coastal marine environments. Intact tDOC can absorb sunlight and lead to ecologically harmful "coastal darkening" by shoaling the euphotic zone and altering the spectral quality of light underwater (Aksnes et al., 2009; Martin et al., 2021; Urtizberea et al., 2013). Moreover, a significant fraction of tDOC may undergo remineralization in shelf seas, as shown for the Eurasian Shelf (Kaiser et al., 2017), the North Sea (Painter et al., 2018), the Louisiana Shelf (Fichot & Benner, 2014), and the Sunda Shelf (Wit et al., 2018; Zhou et al., 2021). In some regions, remineralization of tDOC is sufficiently large to cause ocean acidification (Semiletov et al., 2016; Wit et al., 2018; Zhou et al., 2021) and to drive strong sea–to-air CO_2 fluxes (Cai, 2011; Kitidis et al., 2019; Wit et al., 2018; Zhou et al., 2021). However, the *in-situ* rates and extent of tDOC degradation that control these environmental impacts remain poorly constrained.

The degradation of tDOC is influenced by its optical properties. Rich in colored dissolved organic matter (CDOM) (Massicotte et al., 2017), tDOC can absorb ultraviolet and visible solar radiation (Zepp, 2007). Meanwhile, the abundant unsaturated bonds of the tDOC pool are subject to cleavage upon absorbing radiant energy, leading to a series of photochemical

85 reactions (Zika, 1981). These reactions can cause removal of CDOM (i.e., photobleaching)
86 (Helms, Stubbins, et al., 2013; Tzortziou et al., 2007), complete oxidation of tDOC into CO_2
87 (i.e., photo-remineralization) (Allesson et al., 2021; Mopper et al., 1991; Moran et al., 2000),
88 and chemically alter tDOC molecules (i.e., photo-modification) in a way that renders them
89 more labile to microbial degradation (Dittmar et al., 2007; Stubbins et al., 2010, 2017). The
90 findings that tDOC derived from peatlands of the Congo Basin (Spencer et al., 2009;
91 Stubbins et al., 2010) and of Southeast Asia (Martin et al., 2018; Zhou et al., 2021) is highly
92 photo-labile imply that photodegradation can play an important role in the biogeochemical
93 cycling of tropical peatland tDOC.
94
95 Recently, Aarnos et al. (2018) estimated that direct photo-remineralization can cause a loss of
96 18% of the global riverine tDOC flux in the ocean, based on the relationship between tDOC
97 loss and CDOM loss derived from incubation experiments, and the assumption that all
98 riverine CDOM is photochemically destroyed. However, quantification of the *in-situ* rates
99 and the extent of tDOC photodegradation via realistic modeling is challenging because it
100 requires data for the inherent photochemical properties of the tDOC (i.e., photo-lability and
101 apparent quantum yield), the *in-situ* solar irradiance, and the underwater light field; this
102 requires combining data from incubation experiments, field measurements, satellite
103 observations and meteorological models. To date, such modelling has only been performed in
104 a few cases, such as the Lousiana Shelf (Fichot & Benner, 2014) and the Baltic Sea (Aarnos
105 et al., 2012). Fichot & Benner (2014) concluded that direct photo-remineralisation only

106 consumes 8% of the riverine tDOC input. In contrast, Aarnos et al. (2012) found that the
107 annual DOC photoremineralization exceeds the riverine DOC supply in the Baltic, and
108 concluded that photoremineralization is likely an important tDOC sink in the Baltic Sea.
109 However, for most shelf sea regions we have little understanding of *in-situ* tDOC
110 photo-remineralization, which limits our ability to predict how anthropogenically driven
111 changes to tDOC fluxes might impact coastal ecosystems (Ciais et al., 2013). Although
112 modeling frameworks are being developed to represent the biogeochemistry of tDOC across
113 the land-ocean aquatic continuum (Anderson et al., 2019) and to integrate coastal carbon
114 cycling processes in global ocean models (Mathis et al., 2022), appropriate rate constants for
115 tDOC remineralization are still very poorly constrained.
116
117 In this study, we attempt to estimate *in-situ* photodegradation rates for one of the world's
118 hotspots of riverine tDOC export: Southeast Asia. Rivers draining the peatlands in this region
119 deliver ~21 Tg C of tDOC to the Sunda Shelf Sea annually, which could account for ~10% of
120 the global fluvial tDOC flux (Baum et al., 2007; S. Moore et al., 2011). It appears that at least
121 60–70% of this peatland-derived tDOC is rapidly remineralized in the Sunda Shelf Sea after
122 estuarine mixing (Wit et al., 2018; Zhou et al., 2021). Photodegradation might play an
123 important role here because Southeast Asia's peatland tDOC appears to be highly photo-labile
124 (>70% photo-remineralizable) (Martin et al., 2018; Zhou et al., 2021) but much less
125 bio-labile (Nichols & Martin, 2021). In addition, because of the greater solar irradiance
126 year-round in the tropics (Apell & McNeill, 2019), photodegradation might be a stronger

tDOC sink in the Sunda Shelf Sea compared to higher latitudes.

We incubated riverine and shelf water samples with simulated sunlight to determine the photo-degradability and photochemical efficiency (apparent quantum yield) of tDOC remineralization. We then developed a spectrally resolved optical model based on previous work (Aarnos et al., 2012, 2018; Fichot & Benner, 2014) to estimate the *in-situ* rates and extent of tDOC photo-remineralization, and CDOM photobleaching, for two coastal regions of the Sunda Shelf Sea. We further used our results to estimate a simplified photochemical decay constant that can be applied in ocean biogeochemical models using the recently proposed Unified Model of Dissolved Organic Matter model (Anderson et al., 2019). This will assist to integrate tDOC processing into larger-scale carbon cycle models, especially in Southeast Asia.

2 Materials and Methods

2.1 Overview of study area

Southeast Asia's peatlands are found mainly in the coastal lowlands of Sumatra and Borneo (Fig. 1a). The peat-draining rivers deliver tDOC into the Sunda Shelf Sea, where the oceanic currents and movement of tDOC are controlled by the monsoon (Mayer et al., 2018; Susanto et al., 2016). During the Northeast Monsoon (November to February), water flows from the South China Sea into the central shelf sea and flows towards the Java Sea and the Malacca

Strait; during the Southwest Monsoon (May to August), the currents reverse and carry the tDOC input from the Sumatran rivers into the central Sunda Shelf. After a residence for 1–2 years in the shelf sea, the tDOC exits into the open Indian Ocean through the Malacca Strait, the Sunda Strait, or the Lombok Strait.

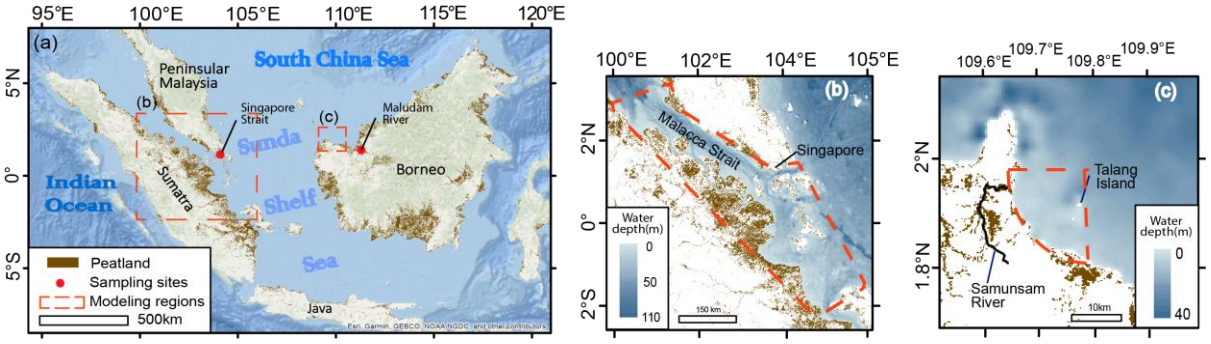

Figure 1. (a) Distribution of peatlands in Southeast Asia and locations of water sampling sites (the Maludam River and the Singapore Strait) and modeling regions. (b) – (c) Red dashed lines encircle the modeling regions, with bathymetry shown: (b) the Southern Malacca Strait (receives input from the Sumatran peatlands) and (c) the Talang Region (receives tDOC input from the Samunsam River). Peatland distribution was obtained from the Center for International Forestry Research, Indonesia (https://www2.cifor.org/global-wetlands/). Bathymetry data were obtained from the GEBCO_2020 grid (GEBCO Compilation Group, 2020).

2.1.1 Sampling sites and water collection for photodegradation experiments

To obtain photochemical data of peatland tDOC, we collected two surface water samples (0–

1 m depth) from the Maludam River (1.636°N 111.049°E) in Sarawak, Borneo in December 2017 and June 2019 and one from the Singapore Strait (1.226°N, 103.860°E) in the coastal Sunda Shelf Sea in July 2020 (Figure 1). The Maludam River samples were gravity-filtered through pre-rinsed 0.22 μm pore-size Whatman Polycap filters on the day of collection and filtered again through pre-rinsed 0.22 μm pore-size polyethersulfone membrane filters upon arrival at Nanyang Technological University, Singapore. The Singapore Strait shelf water sample was filtered through pre-rinsed 0.22 μm pore-size polyethersulfone membrane filters on the day of collection. All filtered water samples were kept at 4°C in the dark and filtered again through pre-rinsed 0.22 μm pore-size polyethersulfone membrane filters before experiments.

Samples from these two sites are representative of the tDOC exported from peatlands into our modeling regions of the coastal ocean, because multiple lines of evidence suggest that the underlying optical and photochemical characteristics of tDOC are similar across the peatlands of Southeast Asia. The Maludam River drains one of the largest remaining intact peatlands in Malaysia, and its catchment consists exclusively of peatlands (Müller et al., 2015). The Maludam samples therefore allow us to obtain AQY estimates for tDOC that is freshly released from a peatland, and that are not influenced by contributions of DOC from other soil types or anthropogenic input. In contrast, the Singapore Strait receives substantial tDOC input from Sumatran peatlands between May and September when tDOC comprises ~50% of the bulk DOC pool, but this tDOC has already undergone fairly extensive remineralization

prior to reaching the Singapore Strait (Zhou et al. 2021). This allows us to estimate the AQY for peatland tDOC that has already undergone some degree of biogeochemical processing in the shelf sea. As a purely peatland-draining river, the Maludam has high DOC concentrations (3000–4000 μmol l^{-1}). Although different rivers across Sumatra and Borneo can vary around 10-fold in DOC concentration, the DOC concentration is linearly related to the proportion of catchment area that is peatland (Rixen et al., 2022). Moreover, across multiple rivers in northwestern Borneo draining catchments with varying peatland proportions and DOC concentrations, there is a strong and linear relationship between DOC concentration and CDOM absorption (Fig. S1, data from (Martin et al., 2018)). This suggests that the concentration of tDOC varies according to the extent of peatland cover in a catchment, but that the optical properties of the tDOC pool are then very similar across rivers, including the Maludam. In addition, the stable carbon isotope composition of DOC ($\delta^{13}C_{DOC}$) is very similar across peatland-draining rivers on Sumatra, Borneo, and Peninsular Malaysia, mostly between -28‰ and -30‰ (data compiled in (Zhou et al., 2021)), and these peatlands share many similarities in plant species (Giesen et al., 2018) and climatic conditions. This further suggests that the photochemical and optical characteristics of the peat-derived tDOC pool should be similar between rivers across the region. This is also supported by our data (see below) that the photochemical efficiency (i.e., apparent quantum yield) of DOC is similar between the Singapore Strait water and the Maludam River water.

208 **2.1.2 Modeling regions**

209 Using our experimental data, we simulated photo-remineralization of tDOC and
210 photobleaching of CDOM for two regions of the Sunda Shelf Sea: the southern Malacca
211 Strait and the Talang Region in Sarawak, Borneo (Fig. 1). Selection of the modeling regions
212 was based on the following considerations. First, both regions receive large riverine input of
213 tDOC from peatlands (Martin et al., 2018; Wit et al., 2018; Zhou et al., 2019, 2021). Second,
214 previous work has indicated the possibility of a significant contribution of photodegradation
215 in both regions: it potentially drives a major part of the tDOC remineralization observed in
216 the shelf sea (Zhou et al., 2021) and the removal of terrigenous CDOM (Kaushal et al., 2021).
217 Third, measurements of the water column inherent optical properties (i.e., particulate
218 absorption and backscattering) are available for both regions (Cherukuru et al., 2021; Martin
219 et al., 2021).

220

221 We ran simulations over different durations for the two regions to accomplish two different
222 objectives. The simulation for the southern Malacca Strait aimed to quantify the contribution
223 of photodegradation to the total quantity of tDOC remineralization observed in this region of
224 the shelf sea, where the water residence time is up to approximately 2 years (Mayer et al.,
225 2015). In contrast, the simulation for the Talang Region aimed to test whether photobleaching
226 of tDOC is sufficiently rapid to contribute to the seasonal variability of CDOM observed at
227 the Talang Islands (Kaushal et al., 2021), where the water residence time is much shorter
228 (Mayer et al., 2015).

The southern Malacca Strait encompasses the shelf waters near the largest peatland area on Sumatra, including the southern part of the Malacca Strait, the Singapore Strait, and the waters to the north of Bangka Island, Indonesia (Fig. 1b). It receives substantial terrestrial input from the Sumatran peatlands by riverine runoff, and it was found that 60–70% of the tDOC is remineralized on the shelf (Wit et al., 2018; Zhou et al., 2021). Based on the water residence time of 1–2 years within this region of the Sunda Shelf (Mayer et al., 2015), we simulated photodegradation for 2 years to quantify a likely upper boundary for the photochemical contribution to the total quantity of tDOC remineralization.

Waters in the Talang Region in Sarawak receive peatland tDOC input carried by the Samunsam River (Fig. 1c). Skeletal luminescence in a coral core from the Talang Island showed seasonal variability terrigenous CDOM levels, with very low values during the Southwest Monsoon (May to August) (Kaushal et al., 2021). This seasonal decrease in the CDOM signal in coral skeletons was argued to be greater than the expected seasonal decrease in the riverine CDOM flux, but closely matched the seasonal changes in solar irradiance (higher during Southwest Monsoon, Fig. S2d). This might indicate a significant role for photodegradation in removing more tDOC and CDOM in the coastal waters during Southwest Monsoon (Kaushal et al., 2021). To test this hypothesis, we estimated the photo-remineralization and photobleaching for different periods of the year.

2.2 Photodegradation experiments for AQY determination

We performed four photodegradation experiments (Exp 1, 2, 3, and 4 below, Table 1) with the water samples from the Maludam River and the Singapore Strait. The changes in DOC concentration and CDOM during Exp 1 and Exp 3 were reported previously (Zhou et al., 2021). Here, we use the data further to calculate the AQY.

In Exp 1, we aimed to quantify the proportion of the peatland-derived tDOC that is photo-remineralizable and to calculate the AQY. We incubated the Maludam sample collected in December 2017 with simulated sunlight, monitored the DOC concentration and CDOM absorption over time, and terminated the experiment when no additional DOC loss was observed (after 816 hours). However, photo-flocculation of DOC was observed at 525 hours, so we only used the data up until the previous time point at 416 hours to calculate the AQY.

In Exp 2, we aimed to quantify the AQY after simulating the mixing of tDOC into the coastal ocean. We diluted 65 ml of the Maludam sample collected in June 2019 with 935 ml of artificial seawater (0.2 g $NaHCO_3$ [Sigma-Aldrich S6014] and 32.09 g NaCl [Sigma-Aldrich S9888] in 1 L ultrapure deionized water [18.2 MΩ cm^{-1}]), achieving a salinity of ~29. We exposed the mixed sample to simulated sunlight, monitored the changes in DOC and CDOM, and terminated the experiment after >25% of DOC was lost (462 hours).

In Exp 3, we aimed to quantify the proportion of tDOC in the shelf water that was still photo-remineralizable after it had already experienced extensive prior degradation in the environment (Zhou et al., 2021). We incubated the Singapore Strait sample with simulated sunlight until no additional DOC loss was observed, which was after 500 hours. Because we previously found that a marine DOC-dominated sample of shelf seawater from Singapore Strait (sample collected in January when there was little tDOC input) showed no photochemical loss of DOC (Fig. 7i in Zhou et al. 2021), the loss of DOC observed in Exp 3 was attributed entirely to photochemical loss of tDOC.

In Exp 4, we aimed to further constrain the AQY of tDOC with a spectrally resolved experiment. We incubated the Maludam sample collected in June 2019 with simulated sunlight under Schott long-pass filters with cut-offs at 295nm, 320nm, 395nm, 420nm, and 455nm. We terminated the experiment after 144 hours, once the DOC and CDOM loss were sufficiently large to calculate the AQY.

Table 1. Summary of the four photodegradation experiments.

	Sample	Duration (hour)
Exp 1	Maludam River water (Dec 2017)	416
Exp 2	Maludam River water (June 2019) diluted with artificial seawater	462

Exp 3	Shelf water during tDOC input (July 2020)	500
Exp 4	Maludam River water (June 2019) with optical cut-off filters	144

288

289

290 In all four experiments, water samples (30 ml) were filled into 14 replicate cylindrical quartz
291 cells (Starna Cells, 50 mm pathlength, 50 mm diameter, with Teflon screw caps) and
292 irradiated in an Atlas Suntest CPS+ solar simulator with a daylight optical filter with
293 integrated irradiance of 40 W m^{-2} between 300–400 nm; the chamber temperature was
294 fan-cooled to below 40°C (the lowest-possible temperature setting). The vertical walls of the
295 quartz cells and bottom of the chamber were covered with black cardboard. A dark control
296 sample was placed in the chamber in a glass bottle wrapped in aluminum foil. At regular time
297 intervals, one or two of the 14 replicates were sacrificed to measure DOC and CDOM to give
298 a time series for each experiment. The long total duration of our experiments was designed
299 for our specific goal of quantifying what proportion of an initial input of tDOC is
300 photo-remineralized cumulatively over its residence time of up to 2 years in the shelf sea (see
301 Section 2.5). We therefore needed the AQY that corresponds to a similar proportion of tDOC
302 loss to what the model ultimately predicts (which is around 20%, Section 3.3), but not the
303 initial AQY determined from very short exposure times (which would be needed to predict
304 instantaneous daily rates of photochemical CO_2 production, which is not our objective).
305 Because each experiment yielded a time series of DOC and CDOM loss we could also test

whether the AQY changed systematically over time, which was not the case.

The irradiance spectrum of the solar simulator was measured with an Ocean Insights FLAME radiometer from 177 nm to 872 nm at 1 nm resolution. We conducted nitrite actinometry following Jankowski et al. (1999) using the same experimental conditions as for our tDOC samples, and found <6% difference between measured and predicted salicylic acid production (Table S1). This showed that the irradiance measured by the radiometer and used for our AQY determination provided an accurate estimate of the irradiance received by our tDOC samples.

2.3 Sample analysis

CDOM absorbance was measured from 230 – 900 nm at room temperature on a Thermo Evolution300 dual-beam spectrophotometer against ultrapure deionized water as a reference using quartz cuvettes with pathlengths of 2, 10 or 100 mm, depending on sample absorbance. The spectra were baseline-corrected, smoothed, and converted to Napierian absorption coefficients using the R package hyperSpec (Beleites & Sergo, 2012). We report the absorption coefficient at 350 nm (a_{350}) as a measure of the CDOM concentration. The spectral slope between 275–295 nm ($S_{275\text{-}295}$) and the specific ultraviolet absorption at 254 nm ($SUVA_{254}$) were used as proxies for DOC apparent molecular weight (Helms et al., 2008) and aromaticity (Weishaar et al., 2003), respectively.

DOC samples (30 ml) were acidified with 100 µl 50% H_2SO_4 and analyzed on a Shimadzu TOC-L system with a high-salt combustion kit as previously described in Zhou et al. (2021). The analytical accuracy was monitored using deep-sea water certified reference material (CRM) (42–45 µmol L^{-1} DOC, University of Miami, USA; long-term mean and standard deviation were 48.0 ± 3.9 µmol L^{-1}).

2.4 Apparent quantum yield calculations

The apparent quantum yield (AQY) can be reported either as a broadband AQY or a spectrally resolved AQY. The broadband AQY is a single value representing the quantity of lost reactant divided by the number of absorbed photons across a specific wavelength range (between 290 and 700 nm in this study), so it shows the "average" photochemical efficiency across this wavelength range. However, the photochemical efficiency varies spectrally. Hence, the spectrally resolved AQY is also frequently reported (Aarnos et al., 2018; Vähätalo et al., 2000, 2003; Zepp, 2007). We calculated both the broadband and spectrally resolved AQY for tDOC and CDOM as summarized below (full details in the Supporting Information).

The spectrally resolved AQY for tDOC photo-remineralization, $\phi_{DOC}(\lambda)$, was assumed to decrease exponentially with increasing wavelength λ (Gao & Zepp, 1998; Koehler et al., 2022; Vähätalo et al., 2000):

$$\phi_{DOC}(\lambda) = c\, e^{-d\lambda} \quad (1)$$

where c (mol C (mol photons)$^{-1}$ nm^{-1}) and d (nm^{-1}) are positive constants. Because the

quantity of photo-remineralized DOC is the product of AQY and the number of absorbed photons $\Xi(\lambda)$:

$$\Delta DOC = \int_{300nm}^{700nm} \phi_{DOC}(\lambda)\, \Xi(\lambda)\, d\lambda \qquad (2),$$

the constants *c* and *d* of $\phi_{DOC}(\lambda)$ can be optimized by iteration until the smallest difference between the left (i.e., the measured DOC loss after irradiation) and the right side (i.e., the predicted DOC loss) of Eqn. 2 is reached. For Exp 1, 2 and 3, the AQY was optimized using data of a single irradiance spectrum and a single value of measured DOC loss following Aarnos et al. (2018) and Aarnos et al. (2012). For Exp 4 where multiple spectral treatments were applied, the AQY was optimized when the smallest sum of squared error between the predicted and the measured DOC loss of all spectral treatments was achieved following Powers et al. (2017). We note that in cases where only a single measurement of DOC loss is available (i.e. Exp 1–3), the shape of the calculated AQY spectrum is sensitive to the choice of starting values for constant *c*. We selected a starting value of 1.0 following Aarnos et al. (2012, 2018), but we also performed a sensitivity analysis in which we repeated our AQY and model calculations using starting values for *c* of 0.01 and of 100.

To also model the photobleaching of CDOM, we extended the concept of AQY to the light dose-dependent decrease in CDOM absorption. We refer to this as $\phi_{CDOM}(\lambda)$, which is the spectrally resolved AQY for the decrease in the volume-integrated CDOM absorption coefficient, with units of L m^{-1} (mol photons)$^{-1}$ nm^{-1}. We assumed that $\phi_{CDOM}(\lambda)$ resembles $\phi_{DOC}(\lambda)$, decreasing exponentially with increasing wavelength λ:

$$\phi_{CDOM}(\lambda) = c' e^{-d'\lambda} \quad (3)$$

where c' (L m^{-1} nm^{-1}) and d' (nm^{-1}) are positive constants. Similar to DOC, the quantity of lost CDOM is the product of AQY and number of absorbed photons $\Xi(\lambda)$:

$$\Delta CDOM = \int_{300nm}^{700nm} \phi_{CDOM}(\lambda)\, \Xi(\lambda)\, d\lambda \quad (4),$$

so the constants c' and d' of $\phi_{CDOM}(\lambda)$ were optimized by iteration until the smallest difference between the left and the right side of Eqn. 4 was reached. The quantity of CDOM is measured as the absorption coefficient times the sample volume, we therefore calculated the AQY in terms of the measured decrease in absorption coefficient across the CDOM absorption spectrum at 1-nm resolution from 250–700 nm. For Exp 1 – 3, we used a single irradiance spectrum for the calculation of AQY; for Exp 4, we used the data from multiple spectral treatments for the calculation of AQY. These calculations are essentially the same as for DOC, but were carried out at every wavelength at which CDOM absorption was measured (from a_{250} to a_{700}) and then concatenated, yielding spectrally-resolved AQY across the CDOM absorption spectrum.

2.5 Model simulation of tDOC photodegradation

2.5.1 Model overview

Our model calculates the daily changes in tDOC concentration and CDOM absorption caused by solar radiation for both regions. Our modeling approach was modified from Fichot & Benner (2014) and Fichot & Miller (2010), but using spectrally resolved AQY as in (Koehler et al., 2022) and extended to explicitly quantify the decrease in CDOM absorption due to

390 photobleaching. This allows a more accurate calculation of the number of absorbed photons
391 as the CDOM absorption decreases over time. The modeling approach is summarized in Fig.
392 2 and below, and is explained in detail in the Supporting Information.
393
394 Our model iteratively calculates (i) hourly solar irradiance just below the water surface based
395 on the above-water irradiance and solar zenith angle, (ii) underwater light attenuation, (iii)
396 daily total number of absorbed photons based on the real-time CDOM absorption, light
397 attenuation and water depth, (iv) daily decrease in DOC concentration and CDOM absorption
398 based on the total absorbed photons over 24 hours and the AQY, and (v) the DOC
399 concentration and CDOM absorption at the end of the day.
400
401 The model simulation was performed first using cloud-corrected solar irradiance to estimate
402 the most realistic photodegradation rates and extent, and then using clear-sky solar irradiance
403 to estimate the maximum possible extent of photodegradation. The uncertainty was estimated
404 by a Monte Carlo approach, where all input parameters were perturbed with a 1σ normally
405 distributed error, the model was recalculated 1,000 times, and the standard deviation of the
406 model outputs was then taken as the estimated uncertainty.
407
408 We used the spectrally resolved AQY calculated from our experimental data for the model
409 simulation, but we also ran the simulation using the broadband AQY for comparison. As we
410 discuss in Section 4.2, using the broadband AQY for our simulation appears to lead to a

significant overestimate of tDOC photoremineralization because of the spectral change in underwater irradiance with depth.

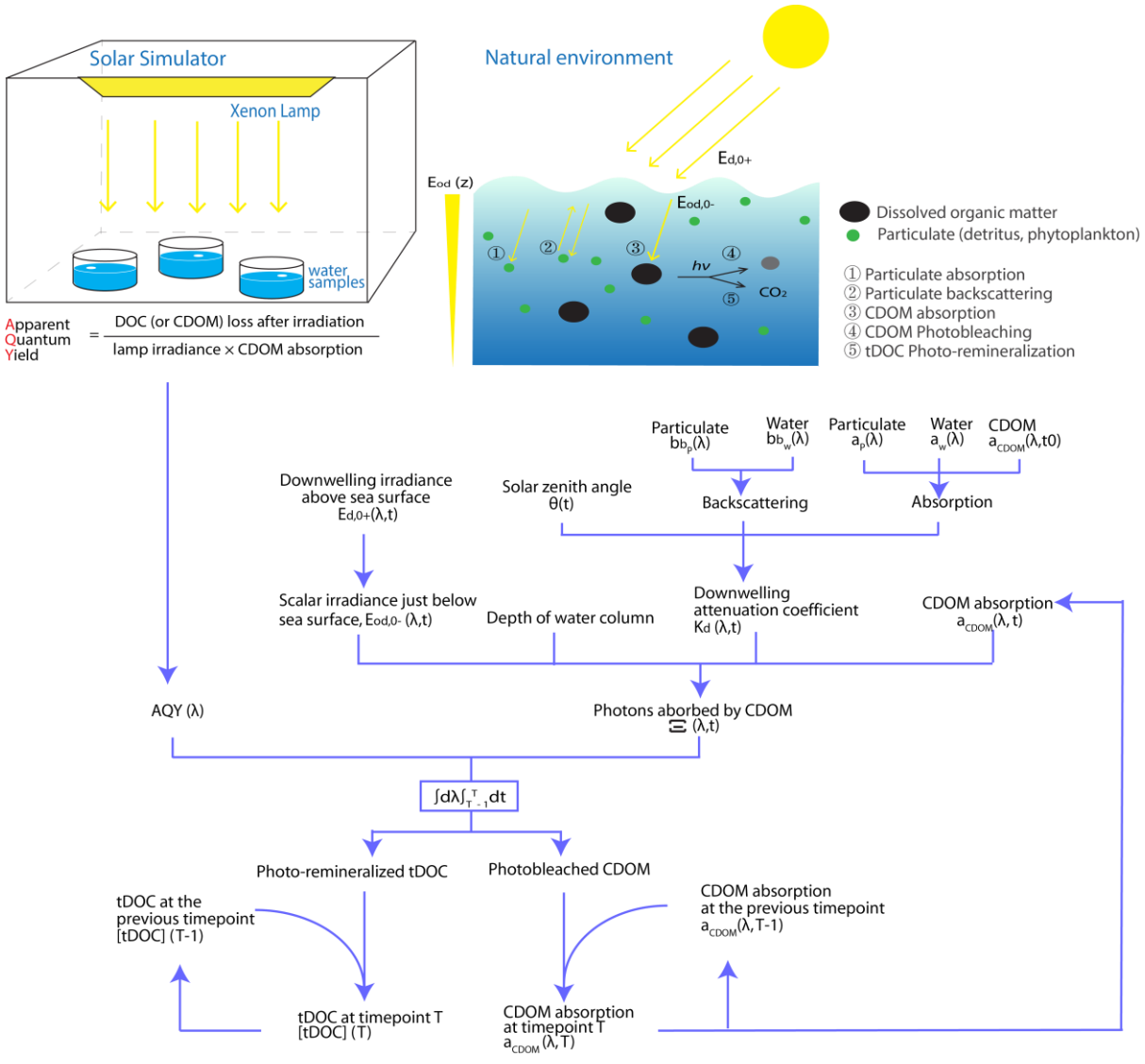

Figure 2. Schematic diagram of the model structure for photodegradation simulation. Input variables, parameters, modeling steps, and the model output are shown here. Time-dependent input variables are labeled with a time variable *t*. Variables are defined in Table S2.

420

421

422

423 **2.5.2 Model input**

424 We used the mean and standard deviation (±1SD) of the four AQY spectra from Exp 1–4 as
425 the model input AQY and its uncertainty, respectively. We obtained the hourly above-water
426 solar irradiance for each month for both modeling regions from the Tropospheric Ultraviolet
427 and Visible Radiation Model (TUV model), US National Center for Atmospheric Research,
428 which were then converted to the irradiance just below the water surface following Fichot
429 and Miller (2010) (Supporting Information). The mean water depth is 19.7 m for the Southern
430 Malacca Strait area and 7.6 m for the Talang region, based on the GEBCO bathymetry
431 (GEBCO Compilation Group, 2020). The areas of the two modeling regions for calculating
432 the mean water depth are shown in Fig. 1b–c. The starting values (i.e., Day 0 values) of
433 tDOC concentration and CDOM absorption were calculated by a two-endmember mixing
434 model using the appropriate riverine endmember data from Wit et al. (2018) and Martin et al.
435 (2018) for the two regions and marine endmember data from Zhou et al. (2021) (Supporting
436 Information). The *in-situ* particulate absorption and backscattering data measured in the
437 Singapore Strait and from the Talang Region were obtained from Martin et al. (2021) and
438 Cherukuru et al. (2021), respectively, and were processed into spectra with 1-nm resolution
439 (Supporting Information). The *in-situ* solar irradiance in each month, initial CDOM spectra
440 (i.e., Day 0) and the particulate absorption and backscattering spectra with their associated

uncertainties are shown in Fig. S3 for both modeling regions. In particular, the Talang Region showed pronounced seasonality in solar irradiance – the greater cloud cover during the NE Monsoon (November to January) drives a decrease in the solar irradiance during that period.

2.5.3 Photochemical decay constant for UniDOM

Anderson et al. (2019) recently proposed the UniDOM framework to model large-scale tDOC biogeochemical processing along the aquatic continuum. The photodegradation component of UniDOM requires a maximum photochemical decay constant, $\emptyset^{ref}$, which defines the photo-remineralization rate of tDOC at the water surface, as the model input. The $\emptyset^{ref}$ is a function of the tDOC photochemical properties and thus is region-specific. We calculated the $\emptyset^{ref}$ for our two regions based on our modeling results. We first calculated the depth-normalized photochemical decay constant, $\emptyset$, based on the modeled loss of DOC over time and then converted the $\emptyset$ to $\emptyset^{ref}$ based on equations in Anderson et al. (2019). Details are given in Supporting Information.

3 Results

3.1 Photodegradability of peatland-derived tDOC

In all four experiments, we observed loss of DOC and CDOM (as absorption at 350nm, a_{350}) upon irradiation, but to different extents (Fig. 3). In Exp 1, flocs were observed at 525 h,

462 suggesting that some DOC was photo-flocculated (Chen et al., 2014; Helms, Mao, et al.,
463 2013) rather than photo-remineralized; we therefore only used the data up to 416 h. The
464 Maludam River water samples showed a greater loss of DOC (26–74% loss) compared to the
465 shelf water sample (9% loss) despite similar duration of irradiation, but they both showed a
466 near-complete removal of CDOM (Fig. 3 & Table S3). In Exp 4, greater loss of DOC and
467 CDOM was observed in the spectral treatments with lower cut-off wavelengths.
468
469

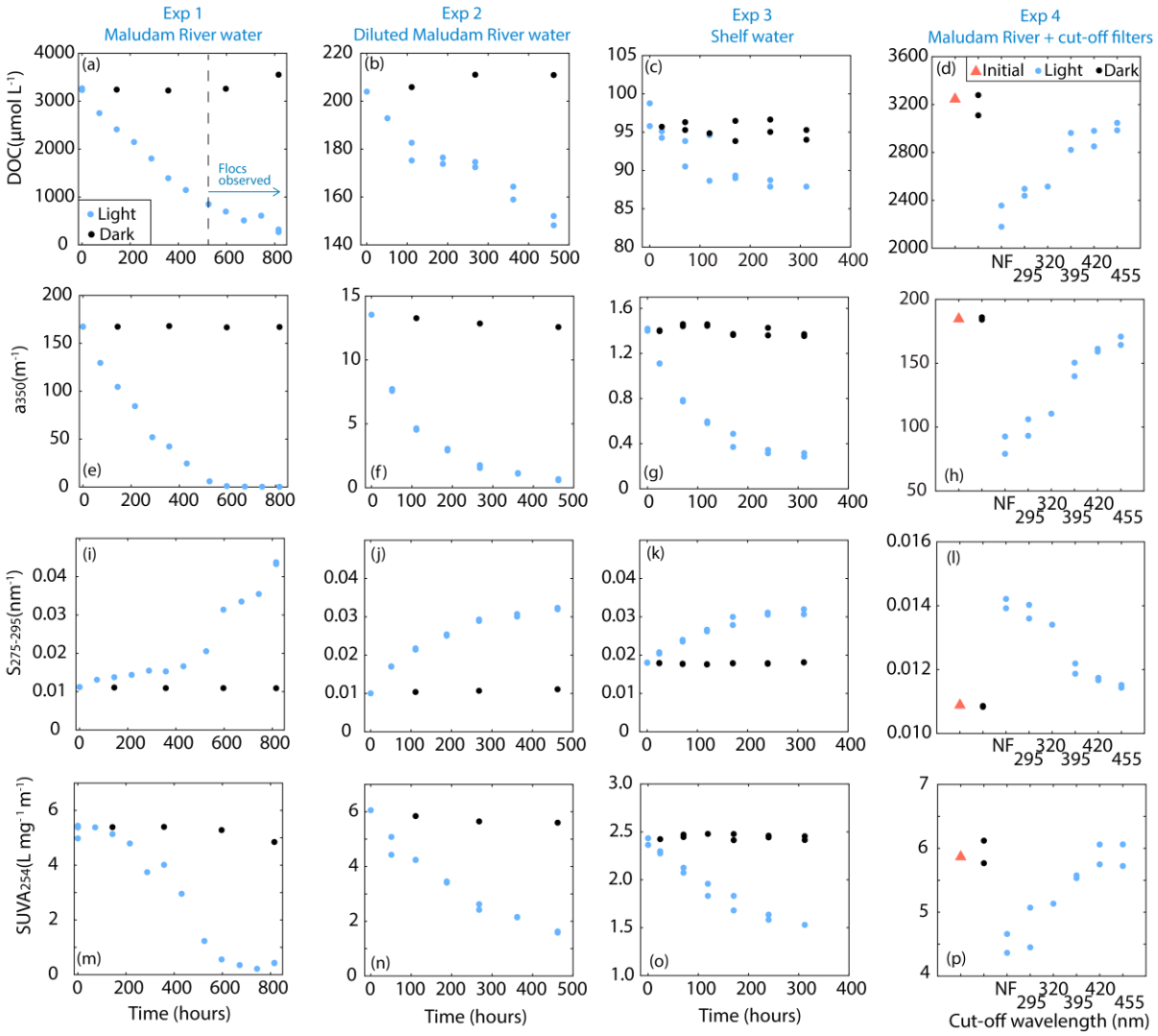

470
471 Figure 3. Changes in DOC concentration and CDOM absorption over time (Exp 1,2, and 3)

and upon irradiation by different wavelength ranges (Exp 4). In Exp 4, the irradiance below the respective cut-off wavelengths was blocked. *NF*: no optical cut-off filter was used.

In all experiments, the CDOM spectral slope between 275 nm and 295 nm ($S_{275\text{-}295}$) increased while the DOC-specific absorbance at 254 nm ($SUVA_{254}$) decreased (Fig. 3 & Table S3), indicating that compounds with high apparent molecular weight and aromatic moieties were preferentially removed upon irradiation (Helms et al., 2008; Weishaar et al., 2003). In Exp 4, the extent of these changes was greater in treatments exposed to lower wavelengths.

3.2 Apparent quantum yield

The broadband AQY was 42–95 μmol C (mol photons)$^{-1}$ for the Maludam River (Exp 1, 2, and 4) and 85 μmol C (mol photons)$^{-1}$ for the shelf seawater tDOC from the Singapore Strait (Exp. 4), which had experienced prior degradation. The AQY did not show a decreasing trend over the course of the experiments (Table S4). Fig. 4a shows the individual AQY spectra for DOC photo-remineralization that we calculated from Exp 1–4, and the mean spectrum. Some previous studies report the AQY at 330 nm irradiance, $\phi_{DOC}(330nm)$, for comparison of the photochemical efficiency between samples. From our data, the $\phi_{DOC}(330nm)$ was 129 – 440 μmol C (mol photons)$^{-1}$ for peatland tDOC from the Maludam River, and 200 μmol C (mol photons)$^{-1}$ for the tDOC in the shelf water from the Singapore Strait. To verify that the optimization procedure for calculating spectrally resolved AQY was successful, we used the calculated spectrally resolved AQY with the irradiance spectrum of the solar simulator to

predict DOC loss, which well reproduced the DOC loss measured in our all four experiments (Fig. S4).

The corresponding AQY spectra for CDOM photobleaching ($\phi_{CDOM}(\lambda)$) are shown in Fig. S2, and the mean spectrum is shown in Fig. 4b. At any given irradiance wavelength, the AQY was higher at shorter wavelengths of the CDOM absorption spectrum. In other words, one mole of photons at a given irradiance wavelength causes a larger decrease in CDOM absorption at a shorter absorption wavelength (for instance, a_{300}) compared to at a longer absorption wavelength (for instance, a_{350}). At any given CDOM absorption wavelength, the AQY decreases exponentially with increasing irradiance wavelength.

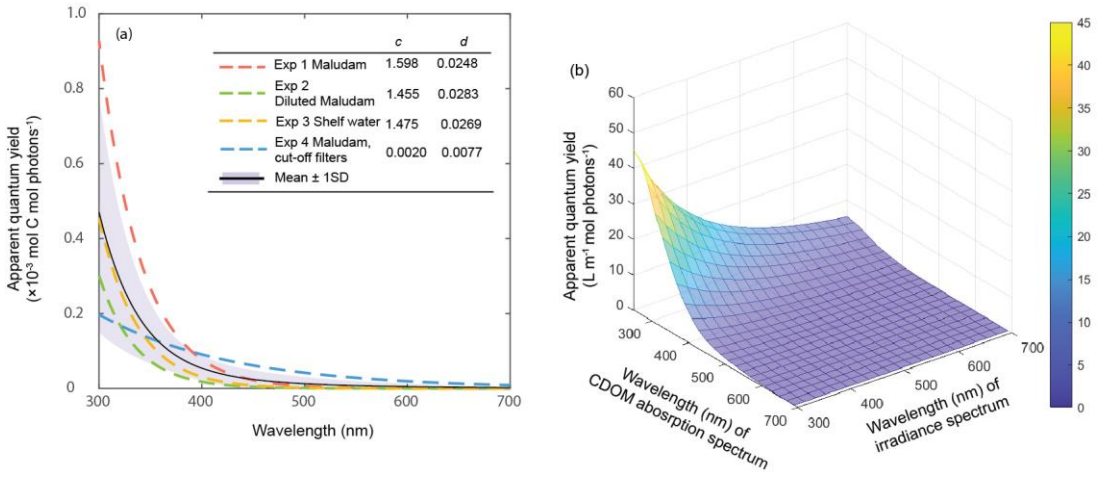

Figure 4. Spectrally resolved apparent quantum yield for (a) tDOC photo-remineralization and (b) CDOM photobleaching (i.e. the AQY for reducing the volume-integrated absorption coefficient). In (a), the individual data from Exp 1–4 are shown together with the mean

spectrum and its standard deviation. In (b), only the mean spectrum is shown for clarity, but the standard deviation of the CDOM photobleaching AQY is included in Supplementary Data Set 1.

3.4 Photodegradation in the southern Malacca Strait

In the cloud-corrected simulation for the southern Malacca Strait, our model predicted that photoremineralization over 2 years reduced the initial tDOC by 20 ± 11% from 108 μmol L^{-1} to 86 ± 12 μmol L^{-1}, while the initial CDOM a_{350} was reduced by 69 ± 5% from 5.6 m^{-1} to 1.7 ± 0.3 m^{-1} (Fig. 5a–b, Table 2). Under clear-sky conditions, 28 ± 16% of tDOC was photo-remineralized and 98 ± 4% of CDOM was photobleached, with a decrease in tDOC concentration from initially 108 μmol L^{-1} to 78 ± 17 μmol L^{-1} and a decrease in a_{350} from 5.6 m^{-1} to 0.13 ± 0.2 m^{-1} (Fig. 5a–b). Our clear-sky simulation represents a maximum possible extent of tDOC photodegradation.

The areal rate of tDOC photo-remineralization (pr_{DOC}) showed seasonal variation according to the seasonality in solar irradiance (Fig. 5c, Fig. S3c). Our results show that 51% of solar irradiance (integrated over 300–700 nm) was absorbed by CDOM on Day 1, but this percentage dropped to 34% (cloud-corrected conditions) and 8% (clear-sky conditions) by the end of the 2-year simulation period (Fig. 5d).

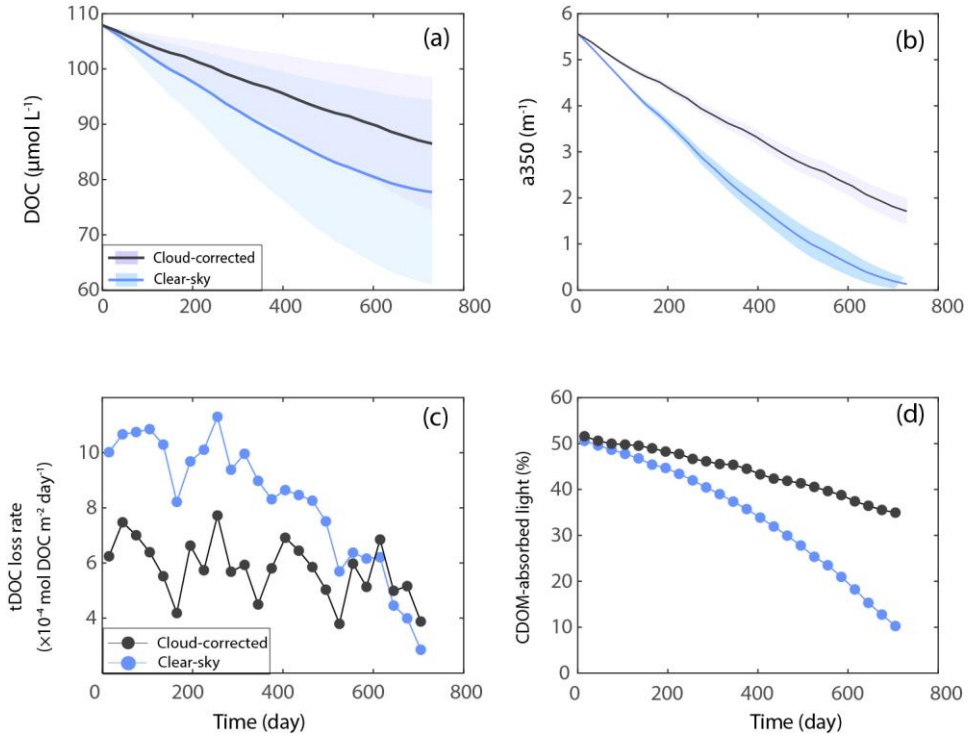

Figure 5. Simulated photodegradation for the southern Malacca Strait. (a) Changes in DOC concentration and (b) CDOM absorption (a_{350}) due to solar radiation under cloud-corrected and clear-sky conditions over our 2-year simulation. The shading represents the model uncertainty as estimated by Monte Carlo simulation. (c) Temporal changes in the photo-remineralization rate. (d) Decrease in the percentage of irradiance (integrated over 300–700 nm) absorbed by CDOM over time due to CDOM photobleaching.

Using the results of Year 1 under the cloud-corrected conditions, we calculated the monthly depth-normalized photochemical decay constant, $\emptyset$, which was 0.0002–0.0003 day^{-1}. The maximum photochemical decay constant, or the decay constant at the water surface, $\emptyset^{ref}$, was 0.008–0.017 day^{-1} with a mean of 0.012 day^{-1} for the southern Malacca Strait. This value could be used to parameterize the UniDOM framework when modeling tDOC turnover for

546 this region.

547

548 To provide a comparison, we also ran a simulation in which we used the broadband AQY
549 instead of the spectrally resolved AQY. The simulation with broadband AQY predicted
550 almost twice as much photodegradation as the simulation with spectrally resolved AQY, with
551 photochemical tDOC loss of 42% (cloud-corrected) and 58% (clear-sky) over two years
552 (Table S5), but we consider this to be an overestimate (see Section 4.2).

553

554 **3.5 The Talang Region**

555 We modeled tDOC photodegradation for four 3-month periods (i.e., February to April, May
556 to July, August to October, and November to January) for the Talang Region, which are the
557 periods showing greatest seasonal differences in solar irradiance (Fig. 6, Table 2). Our model
558 predicted that after 3 months under cloud-corrected conditions, DOC concentration decreased
559 from initially 181 μmol L^{-1} to 173–176 μmol L^{-1}, or by 3–4%; the CDOM a_{350} decreased
560 from 10.3 m^{-1} to between 8.7–9.3 m^{-1}, or by 10–15%. Photobleaching of CDOM exhibited
561 pronounced seasonal variation: the early Southwest Monsoon (May to July, when solar
562 irradiance is highest) showed the greatest removal of CDOM (15% loss) while the Northeast
563 Monsoon (November to January) showed the smallest removal (10% loss). Under clear-sky
564 conditions, DOC concentration decreased from initially 181 μmol L^{-1} to 167 μmol L^{-1}, or by
565 8%, and the a_{350} of CDOM decreased from 10.3 m^{-1} to 7.3–7.5 m^{-1}, or by 28%, after 3 months.
566 The uncertainty in the final DOC concentration and a_{350} as estimated from our Monte Carlo

567 approach was ±2–4 μmol L^{-1} and ±0.1 m^{-1}, respectively.

568

569 The areal rate of DOC photo-remineralization was 3–7.6 $\times 10^{-4}$ mol m^{-2} day^{-1} under
570 cloud-corrected conditions and 10–12 $\times 10^{-4}$ mol m^{-2} day^{-1} under clear-sky conditions
571 (Fig. 6i–l).. Seasonal variation in photoremineralization rate was greater in the
572 cloud-corrected simulation, and the rate was lowest during the NE Monsoon and highest
573 during the early SW Monsoon. The depth-normalized photochemical decay constant, $\emptyset$, was
574 0.0003–0.0005 day^{-1}, which returned a photochemical decay constant at the water surface,
575 $\emptyset^{ref}$, of 0.007–0.018 day^{-1} with a mean of 0.013 day^{-1}.

576

577

578

579

580

581

582

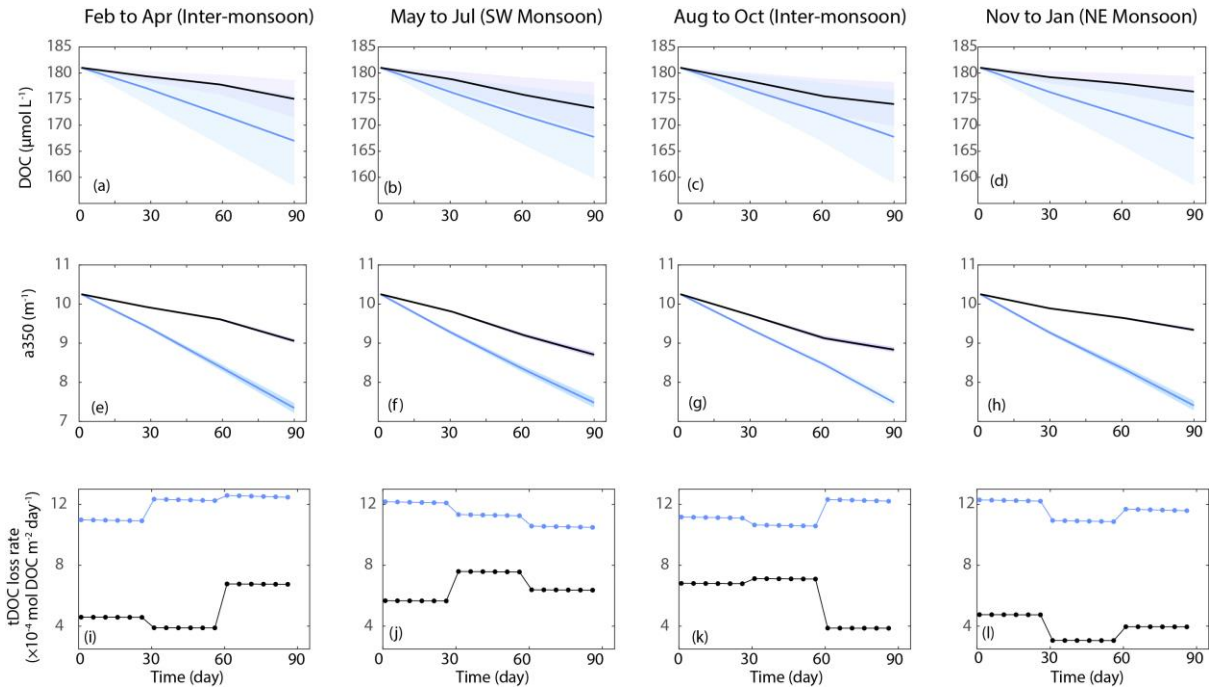

583

584 Figure 6. Simulated photodegradation for the Talang Region. (a)–(d) Changes in DOC
585 concentrations and (e)–(h) Changes in the CDOM absorption (a_{350}) under cloud-corrected
586 and clear-sky conditions for three months in different periods of the year. The grey shading
587 represents the uncertainties as estimated from the Monte Carlo simulation. (i)–(l) Seasonal
588 variation in the modeled *in-situ* photo-remineralization rates.

589

590 Table 2. Summary of simulated photodegradation under the cloud-corrected conditions. For
591 the Talang Region, the range in results obtained for the four different time periods is given.

		Initial	Final	%loss
Southern Malacca Strait (730 days)	DOC (μmol L^{-1})	108	86 ± 10	20 ± 9%
	CDOM a_{350} (m^{-1})	5.6	1.7 ± 0.2	69 ± 4%

Talang Region (90 days)	DOC (μmol L^{-1})	181	173–176	3–4%
	CDOM a_{350} (m^{-1})	10.3	8.7–9.3	10–15%

592

593

594 **4 Discussion**

595 **4.1 Photodegradability of Southeast Asian peat-tDOC**

596 Our experimental results indicate that a high proportion of tDOC from Southeast Asian
597 peatlands is photo-labile, consistent with previous work on tDOC from the
598 peatland-influenced Congo River (Spencer et al., 2009; Stubbins et al., 2010). The shelf water
599 tDOC collected from the Singapore Strait contained a smaller photo-labile fraction (<8% loss
600 OF tDOC), which was expected because the more photo-labile fractions of tDOC had most
601 likely already been remineralized before reaching the Singapore Strait (Zhou et al., 2021).

602

603 We use the photo-remineralization efficiency $\phi_{DOC}(330nm)$ to compare our data to
604 previous literature. Our AQY for Southeast Asian peatland tDOC is comparable to that in
605 large rivers and estuaries globally, but much lower compared to boreal inland waters and
606 oceanic DOC (Table 3). Our AQY is similar to that of Congo River tDOC, which is also
607 partly derived from peatlands (Aarnos et al., 2018), suggesting that tropical peatland tDOC,
608 despite its high photo-lability due to the high aromatic content, is probably not amongst the
609 most efficient organic carbon pools worldwide in the photo-production of CO_2.

610

611 Table 3. Comparison of apparent quantum yield at 330 nm irradiance for tDOC
612 photo-remineralization from this study to values in previous literature.

Study site(s)	$\phi_{DOC}(330nm)$ μmol C mol photons^{-1}	Reference
Maludam River (Peatland-derived DOC)	440 (Exp 1, Maludam River) 129 (Exp 2, diluted Maludam river water) 156 (Exp 4, Maludam River)	This study
Singapore Strait (Southwest Monsoon during seasonal tDOC input)	203	This study
World's major rivers	172–335	Aarnos et al. (2018)
Congo River (Peatland-derived tDOC)	286	Aarnos et al. (2018)
Tropical and temperate lakes	250–750	Koehler et al. (2016)
Delaware Estuary	249	White et al. (2010)
Inshore waters	514	Powers & Miller (2015)
Boreal Lakes	300–2000	Koehler et al. (2014, 2016)
Humic Lake	708	Vähätalo et al. (2000)
Coastal Waters	989	Johannessen & Miller (2001)
Open Ocean	2900	Johannessen & Miller (2001)

613

614

615 **4.2 Limitations of the AQY determination**

616 Our approach for calculating spectrally resolved AQY from our experiments has limitations,
617 but as we show below, these limitations do not affect our modeling results and conclusion.
618 The limitations are: 1) the method assumes that AQY decreases exponentially with increasing
619 wavelength, and 2) the optimized AQY spectrum does not have a unique solution but varies
620 depending on the starting values chosen for the optimization.

621

622 The assumption that AQY spectra have an exponential shape has been validated by
623 measurements of AQY for pure organic molecules at multiple discrete wavelengths (Gao &
624 Zepp, 1998; C. A. Moore et al., 1993; Moran & Zepp, 1997) and is thus reasonable to be
625 extended to the natural organic matter pool (Aarnos et al., 2012; Koehler et al., 2016;
626 Vähätalo et al., 2000). Experiments using wavelength cut-off filters or monochromatic light
627 sources also confirm that AQYs for natural DOC show exponential spectra (Ward et al.,
628 2021).

629

630 To address the impact of the optimization parameters, we ran a sensitivity analysis in which
631 we changed the starting value of coefficient *c* in the AQY calculation from 1.0 (Aarnos et al.,
632 2012, 2018) to first 0.01 and then to 100, and then repeated our model simulation with each
633 of the two resulting AQY spectra. We found that changing the starting values for the

coefficients over this range of 4 orders of magnitude did indeed change the shape of the AQY spectra (Fig. S5), but this only changed our final estimate of how much tDOC is photo-remineralized by < 6% (Table S6). While this rather limited sensitivity of our model result to the shape of the AQY spectrum may seems surprising, it is a consequence of the fact that we are simulating photodegradation in a well-mixed water column that is optically thick, i.e. the incoming solar radiation is nearly all absorbed within the water layer we are simulating. Therefore, with a steeper AQY spectrum our model predicts more DOC loss close to the surface where there is more UV light but less DOC loss deeper down; while with a flatter AQY spectrum, there is less DOC loss at shallow depths but in turn more DOC loss in deeper waters caused by visible wavelengths. It should be noted that if photodegradation is being modeled for a water layer that is optically thinner (e.g. for a surface mixed layer that is shallower than the euphotic zone depth) the uncertainty in AQY spectral shape associated with this optimization calculation could be much more significant.

Despite these limitations, it is important to use a spectral AQY rather than applying a broadband AQY when simulating photodegradation in an optically thick water layer because the irradiance spectrum shifts strongly to longer wavelengths (with lower AQY) within just 1–2 m below the surface in these optically complex waters (Martin et al., 2021). However, the broadband AQY in our experiments was necessarily determined by exposing optically thin tDOC solutions to full-spectrum irradiance. This broadband AQY is only appropriate for calculating photodegradation in a water layer that is similarly optically thin as in the

655 experimental conditions, such that the depth-integrated spectrum of photons absorbed by
656 CDOM has a similar shape between the model and the experiments – but if it is applied in
657 deeper waters where the irradiance spectrum (and the depth-integrated spectrum of photons
658 absorbed by CDOM) is shifted to longer wavelengths, it overestimates the photodegradation.
659 This is illustrated by the fact that when we used the broadband AQY from our experiments to
660 run our model, it predicted around twice as much tDOC loss compared to the simulation with
661 spectrally resolved AQY (see Table S5 and Section 3.3). This clearly represents an
662 overestimate of the tDOC photo-remineralization, because the depth-integrated spectrum of
663 photons absorbed by CDOM for our modeled water column is shifted considerably towards
664 blue and green wavelengths (that have lower AQY than UV light) relative to that in our
665 experiments that are used to calculate the AQY (Fig. S6).
666
667 Finally, our AQY spectra were derived from a limited number of samples. Although the
668 Maludam River and Singapore Strait samples are likely fairly well representative of the
669 peatland tDOC in Southeast Asia (Section 2.1.1), and our uncertainty analysis shows that the
670 variation between these AQY spectra does not result in substantial model uncertainties
671 (Sections 3.4 and 3.5), more AQY determinations should be made for this region.
672
673 **4.3 Contribution of photodegradation to total tDOC remineralization**
674 Previous work showed that at least 60–70% of tDOC exported from Sumatran peatlands is
675 remineralized in the coastal waters of the Sunda Shelf Sea (Wit et al., 2018; Zhou et al.,

676 2021). Given also that the direct microbial remineralization appears to be slow and therefore
677 a minor sink for tDOC over the residence time of tDOC on the shelf, we previously
678 hypothesized that photodegradation accounts for a significant part of this remineralization
679 (Nichols & Martin 2021; Zhou et al. 2021). However, our cloud-corrected model simulation
680 shows that solar radiation can only directly remineralize 20 ± 11% of the initial tDOC input
681 during the 2-year residence time on the shelf. This would account for 31% of the total tDOC
682 remineralization estimated by Zhou et al. (2021). While direct photo-remineralization thus
683 appears to make an important contribution, it is clearly not the only important process. We
684 therefore infer that photochemically enhanced microbial remineralization (Cory et al., 2007;
685 Cory & Kling, 2018; Judd et al., 2007; Moran & Zepp, 1997) might be important in Southeast
686 Asia. Such interactive remineralization was estimated to account for 32% of the total tDOC
687 remineralization on the Louisiana Shelf (Fichot & Benner, 2014). Our photodegradation
688 experiments suggested a preferential removal of tDOC compounds with high apparent
689 molecular weight upon solar radiation, which would be consistent with increased bio-lability
690 of the partially photodegraded tDOC (Miller & Moran, 1997; Moran et al., 2000; Moran &
691 Zepp, 1997). However, photodegradation can also compete with biodegradation for the same
692 tDOC fractions (Ward et al., 2017). Further research is therefore required to quantify the
693 contribution of photo-enhanced bio-remineralization to the tDOC processing.
694
695 In the Talang Region, solar irradiation can only directly remineralize 3–4% of the initial
696 tDOC input over 3 months (given the more open coastline in this region, tDOC will most

likely be removed by mixing and advection over time scales longer than 3 months). This low photodegradation rate from our modeling is consistent with the conservative mixing behavior and the limited degradation of tDOC across peatland-draining estuaries in Southeast Asia reported previously (Alkhatib et al., 2007; Baum et al., 2007; Martin et al., 2018). However, solar radiation removes 7–12% of the riverine CDOM in this region over three months. Photobleaching can therefore remove a significant portion of CDOM over seasonal time scales, as hypothesized by Kaushal et al. (2021). The seasonal variation in the extent of photobleaching observed from our modeling (i.e., greater loss of CDOM during Southwest Monsoon than Northeast Monsoon) is driven by the seasonal changes in irradiance in this region, chiefly due to the seasonality of cloud cover (Fig. S3d), and might contribute to the large seasonal decrease in CDOM after the NE Monsoon inferred from coral skeleton luminescence (Kaushal et al., 2021).

Our modeling results also indicate that photodegradation might play a larger role in tDOC processing in the Sunda Shelf Sea compared to regions at higher latitudes. On the Louisiana Shelf, direct photo-remineralization appears to remove only 4% of the riverine tDOC input within the surface mixed layer, accounting for only 8% of the total tDOC remineralization (Fichot & Benner, 2014). On a global scale, Aarnos et al. (2018) estimated that if all riverine CDOM is photobleached, 18% of the riverine tDOC flux is photo-remineralized in the ocean. That estimate is close to our results that 20% of the Sumatran peatland tDOC is photo-remineralized on the shelf, showing the quantitatively important role of

718 photo-remineralization in the tropical shelf sea in Southeast Asia. The greater relative
719 contribution from photo-remineralization here is likely due to the relatively long water
720 residence time in the shelf sea (2 years) (Mayer et al., 2015), the higher solar irradiance in the
721 tropics (Apell & McNeill, 2019) and the low bio-lability of the tDOC (Nichols & Martin,
722 2021).
723
724 **4.4 Decay constants for simplified photodegradation modeling**
725 Our spectrally resolved optical modeling can potentially inform the parameterization of
726 simplified model representations of terrestrial carbon cycling such as UniDOM (Anderson et
727 al., 2019), which was proposed as a modeling framework that is sufficiently simplified to be
728 included in large-scale Earth System Models. Specifically, we can use our results to estimate
729 the decay rate constants $\emptyset$ and $\emptyset^{ref}$ that are key input variables in UniDOM, so that tDOC
730 photo-remineralization can be modelled realistically in Southeast Asia. The $\emptyset^{ref}$ derived
731 from our modeling results (0.008 – 0.017 day^{-1}) is much smaller than the default global value
732 used in UniDOM (0.13 day^{-1}), which was based on the observed decay rate in laboratory
733 photodegradation experiments. UniDOM applies a large age-dependent term to rapidly
734 decrease the very high initial maximum decay rate over time based on global observations of
735 the decreasing DOC turnover rate with the increasing DOC age (Catalán et al., 2016; Evans
736 et al., 2017) and to yield an overall realistic extent of photo-remineralization. In contrast, our
737 photodegradation experiments did not show a systematic decrease in the photochemical
738 efficiency (i.e., AQY) of tDOC over time (Table S4). This suggests that a large age-dependent

correction might not be the most appropriate way to parameterize photochemical tDOC, provided that realistic *in-situ* values of $\emptyset^{ref}$ can be estimated.

Our data also show that high photo-lability as measured in experimental incubations does not necessarily lead to a high *in-situ* photodegradation rate because the latter is also dependent on the *in-situ* light dose, the depth-integrated total amount of tDOC and CDOM, and other inherent optical properties (IOPs) in the water. For example, our Exp 1 showed that a 22-day simulated solar radiation can cause a loss of 74% of the initial tDOC. However, the *in-situ* solar irradiance (35 mol photons m^{-2} day^{-1}, integrated over 300–700nm) is only one-fifth of the irradiance in the solar simulator (181 mol photons m^{-2} day^{-1}), while the tDOC amount to be remineralized in the entire water column of the shelf sea (2.12 mol m^{-2}) is 35 times of that in each cuvette used in the photodegradation experiments (0.06 mol m^{-2}). The extent of tDOC photo-remineralization on the shelf is also constrained by its residence time. Regarding the IOPs in the water, the particulate absorption and backscattering are lower than the CDOM absorption for both modeled regions, partly because of the low chlorophyll-*a* concentrations in the study region (Martin et al., 2018, 2022). The light attenuation coefficient, K_d, is therefore dominated by CDOM absorption (Martin et al., 2021), especially at ultraviolet wavelengths. Given the multiple controlling factors of *in-situ* photodegradation rates, we recommend performing spectrally resolved optical modeling to obtain more accurate estimates of the photochemical decay rate constant that can then be used by simplified models across much larger scales.

760

761

762 **5 Conclusions**

763 Although the tDOC from Southeast Asian peatlands contains a large photolabile fraction, the
764 apparent quantum yields for tDOC remineralization are fairly low, which is consistent with
765 apparent quantum yields for tDOC reported from major rivers globally. Based on model
766 simulations, we found that (1) natural solar radiation can directly remineralize 20 ± 11% of
767 the tDOC flux from Sumatran peatlands in the shelf sea, but this process alone is insufficient
768 to account for the high reported extent of tDOC remineralization in this region; (2) seasonal
769 variation in photobleaching of terrestrial CDOM probably contributes to the strong
770 seasonality of coral core luminescence records in the Talang Region of northwestern Borneo
771 (Kaushal et al., 2021); (3) our modeled rates of tDOC photo-remineralization are equivalent
772 to using a photochemical decay constant, $\emptyset^{ref}$, of 0.008 – 0.017 day^{-1} in the UniDOM model,
773 but an age-dependent correction factor is not necessary. Our study demonstrates that
774 photochemical processing of peatland tDOC is important in Southeast Asia but falls far short
775 of explaining the extent of tDOC remineralization observed in the Sunda Shelf Sea. We
776 hypothesize that interactions between photochemical and microbial remineralization are
777 likely significant in this region and need to be quantified in future research.

778

779 **Acknowledgements**

780 We are grateful to the many students and research staff, especially from Nanyang

781 Technological University, Swinburne University of Science and Technology, and Universiti
782 Malaysia Sarawak, who helped with field and laboratory work. Permission for this research
783 was given by the National Parks Board, Singapore (permit NP/RP17-044-3), and by the
784 Sarawak Forestry Department and Sarawak Biodiversity Centre (permits
785 NPW.907.4.4(Jld.14)-161, WL83/2017, and SBC-RA-0097-MM). Patrick Martin
786 acknowledges funding by the Singapore Ministry of Education under the Academic Research
787 Fund Tier 2 programme (grant MOE-MOET2EP10121-0007) and by the National Research
788 Foundation Singapore, Prime Minister's Office, as part of the Marine Science Research and
789 Development Programme (grant MSRDP-P32). Moritz Müller was funded by MOHE FRGS
790 15 (grant FRGS/1/2015/WAB08/SWIN/02/1) and by the Newton-Ungku Omar Fund (grant
791 GL/F07/NUOF/01/2017). Nagur Cherukuru was funded by CSIRO Oceans and Atmosphere
792 and by the Regional Collaborations Programme (Australian Academy of Sciences).
793

794 **Open Research**

795 Raw experimental data and source codes for data processing and modeling are available
796 through the NTU data repository (https://doi.org/10.21979/N9/XQSOEN).
797

798 **Author Contributions**

799 Conceptualization: Y.Z., P.M.;

800 Methodology: Y.Z., P.M.;

801 Software: Y.Z.;

Formal analysis: Y.Z.;

Resources: P.M., M.M., N.C.;

Data curation: Y.Z., M.M., N.C., P.M.;

Investigation: Y.Z.;

Writing – original draft preparation: Y.Z.;

Writing – review and editing: Y.Z., M.M., N.C., P.M.;

Supervision: P.M.;

Project administration: P.M.;

Funding acquisition: P.M., M.M., N.C.

References

Aarnos, H., Ylöstalo, P., & Vähätalo, A. V. (2012). Seasonal phototransformation of dissolved organic matter to ammonium, dissolved inorganic carbon, and labile substrates supporting bacterial biomass across the Baltic Sea. *Journal of Geophysical Research: Biogeosciences*, *117*(1), 1–14. https://doi.org/10.1029/2010JG001633

Aarnos, H., Gélinas, Y., Kasurinen, V., Gu, Y., Puupponen, V. M., & Vähätalo, A. V. (2018). Photochemical Mineralization of Terrigenous DOC to Dissolved Inorganic Carbon in Ocean. *Global Biogeochemical Cycles*, *32*(2), 250–266. https://doi.org/10.1002/2017GB005698

Aksnes, D. L., Dupont, N., Staby, A., Fiksen, Ø., Kaartvedt, S., & Aure, J. (2009). Coastal

water darkening and implications for mesopelagic regime shifts in Norwegian fjords. *Marine Ecology Progress Series*, *387*(Jerlov 1968), 39–49. https://doi.org/10.3354/meps08120

Alkhatib, M., Jennerjahn, T. C., & Samiaji, J. (2007). Biogeochemistry of the Dumai River estuary, Sumatra, Indonesia, a tropical black-water river. *Limnology and Oceanography*, *52*(6), 2410–2417. https://doi.org/10.4319/lo.2007.52.6.2410

Allesson, L., Koehler, B., Thrane, J. E., Andersen, T., & Hessen, D. O. (2021). The role of photomineralization for CO2 emissions in boreal lakes along a gradient of dissolved organic matter. *Limnology and Oceanography*, *66*(1), 158–170. https://doi.org/10.1002/lno.11594

Anderson, T. R., Rowe, E. C., Polimene, L., Tipping, E., Evans, C. D., Barry, C. D. G., et al. (2019). Unified concepts for understanding and modelling turnover of dissolved organic matter from freshwaters to the ocean: the UniDOM model. *Biogeochemistry*, *146*(2), 105–123. https://doi.org/10.1007/s10533-019-00621-1

Apell, J. N., & McNeill, K. (2019). Updated and validated solar irradiance reference spectra for estimating environmental photodegradation rates. *Environmental Science: Processes and Impacts*, *21*(3), 427–437. https://doi.org/10.1039/c8em00478a

Baum, A., Rixen, T., & Samiaji, J. (2007). Relevance of peat draining rivers in central Sumatra for the riverine input of dissolved organic carbon into the ocean. *Estuarine, Coastal and Shelf Science*, *73*(3–4), 563–570. https://doi.org/10.1016/j.ecss.2007.02.012

Beleites, C., & Sergo, V. (2012). hyperSpec: a package to handle hyperspectral data sets in R.

Journal of Statistical Software.

Cai, W.-J. (2011). Estuarine and Coastal Ocean Carbon Paradox: CO 2 Sinks or Sites of Terrestrial Carbon Incineration? *Annual Review of Marine Science*, *3*(1), 123–145. https://doi.org/10.1146/annurev-marine-120709-142723

Catalán, N., Marcé, R., Kothawala, D. N., & Tranvik, L. J. (2016). Organic carbon decomposition rates controlled by water retention time across inland waters. *Nature Geoscience*, *9*(7), 501–504. https://doi.org/10.1038/ngeo2720

Chen, H., Abdulla, H. A. N., Sanders, R. L., Myneni, S. C. B., Mopper, K., & Hatcher, P. G. (2014). Production of Black Carbon-like and Aliphatic Molecules from Terrestrial Dissolved Organic Matter in the Presence of Sunlight and Iron. *Environmental Science and Technology Letters*, *1*(10), 399–404. https://doi.org/10.1021/ez5002598

Cherukuru, N., Martin, P., Sanwlani, N., Mujahid, A., & Müller, M. (2021). A semi-analytical optical remote sensing model to estimate suspended sediment and dissolved organic carbon in tropical coastal waters influenced by peatland-draining river discharges off sarawak, borneo. *Remote Sensing*, *13*(1), 1–31. https://doi.org/10.3390/rs13010099

Ciais, P., Sabine, C., & Bala, G. (2013). Chapter 6: Carbon and other biogeochemical cycles. *Climate Change 2013: The Physical Science Basis*.

Cory, R. M., & Kling, G. W. (2018). Interactions between sunlight and microorganisms influence dissolved organic matter degradation along the aquatic continuum. *Limnology and Oceanography Letters*, *3*(3), 102–116. https://doi.org/10.1002/lol2.10060

Cory, R. M., McKnight, D. M., Chin, Y. P., Miller, P., & Jaros, C. L. (2007). Chemical

865 characteristics of fulvic acids from Arctic surface waters: Microbial contributions and
866 photochemical transformations. *Journal of Geophysical Research: Biogeosciences*,
867 *112*(4), 1–14. https://doi.org/10.1029/2006JG000343
868 Dittmar, T., Whitehead, K., Minor, E. C., & Koch, B. P. (2007). Tracing terrigenous dissolved
869 organic matter and its photochemical decay in the ocean by using liquid
870 chromatography/mass spectrometry. *Marine Chemistry*, *107*(3), 378–387.
871 https://doi.org/10.1016/j.marchem.2007.04.006
872 Evans, C. D., Futter, M. N., Moldan, F., Valinia, S., Frogbrook, Z., & Kothawala, D. N.
873 (2017). Variability in organic carbon reactivity across lake residence time and trophic
874 gradients. *Nature Geoscience*, *10*(11), 832–835. https://doi.org/10.1038/NGEO3051
875 Fichot, C. G., & Benner, R. (2014). The fate of terrigenous dissolved organic carbon in a
876 river-influenced ocean margin. *Global Biogeochemical Cycles*, *28*(3), 300–318.
877 https://doi.org/10.1002/2013GB004670
878 Fichot, C. G., & Miller, W. L. (2010). An approach to quantify depth-resolved marine
879 photochemical fluxes using remote sensing: Application to carbon monoxide (CO)
880 photoproduction. *Remote Sensing of Environment*, *114*(7), 1363–1377.
881 https://doi.org/10.1016/j.rse.2010.01.019
882 Gao, H., & Zepp, R. G. (1998). Factors influencing photoreactions of dissolved organic
883 matter in a coastal river of the southeastern United States. *Environmental Science and*
884 *Technology*, *32*(19), 2940–2946. https://doi.org/10.1021/es9803660
885 GEBCO Compilation Group. (2020). GEBCO 2020 Grid.

886 https://doi.org/10.5285/a29c5465-b138-234d-e053-6c86abc040b9
887 Giesen, W., Wijedasa, L. S., & Page, S. E. (2018). Unique Southeast Asian peat swamp forest
888 habitats have relatively few distinctive plant species. *Mires and Peat*, *22*, 1–13.
889 https://doi.org/10.19189/MaP.2017.OMB.287
890 Gu, Y., Lensu, A., Perämäki, S., Ojala, A., & Vähätalo, A. V. (2017). Iron and pH Regulating
891 the Photochemical Mineralization of Dissolved Organic Carbon. *ACS Omega*, *2*(5),
892 1905–1914. https://doi.org/10.1021/acsomega.7b00453
893 Helms, J. R., Stubbins, A., Ritchie, J. D., Minor, E. C., Kieber, D. J., & Mopper, K. (2008).
894 Absorption spectral slopes and slope ratios as indicators of molecular weight, source,
895 and photobleaching of chromophoric dissolved organic matter. *Limnology and*
896 *Oceanography*, *53*(3), 955–969. https://doi.org/10.4319/lo.2008.53.3.0955
897 Helms, J. R., Stubbins, A., Perdue, E. M., Green, N. W., Chen, H., & Mopper, K. (2013).
898 Photochemical bleaching of oceanic dissolved organic matter and its effect on
899 absorption spectral slope and fluorescence. *Marine Chemistry*, *155*, 81–91.
900 https://doi.org/10.1016/j.marchem.2013.05.015
901 Helms, J. R., Mao, J., Schmidt-Rohr, K., Abdulla, H., & Mopper, K. (2013). Photochemical
902 flocculation of terrestrial dissolved organic matter and iron. *Geochimica et*
903 *Cosmochimica Acta*, *121*, 398–413. https://doi.org/10.1016/j.gca.2013.07.025
904 Jankowski, J. J., Kieber, D. J., & Mopper, K. (1999a). Nitrate and nitrite ultraviolet
905 actinometers. *Photochemistry and Photobiology*, *70*(3), 319–328.
906 https://doi.org/10.1111/j.1751-1097.1999.tb08143.x

907 Jankowski, J. J., Kieber, D. J., & Mopper, K. (1999b). Nitrate and Nitrite Ultraviolet
908 Actinometers. *Photochemistry and Photobiology*, *70*(3), 319–328.
909 https://doi.org/10.1111/j.1751-1097.1999.tb08143.x
910 Johannessen, S. C., & Miller, W. L. (2001). Quantum yield for the photochemical production
911 of dissolved inorganic carbon in seawater. *Marine Chemistry*, *76*(4), 271–283.
912 https://doi.org/10.1016/S0304-4203(01)00067-6
913 Judd, K. E., Crump, B. C., & Kling, G. W. (2007). Bacterial responses in activity and
914 community composition to photo-oxidation of dissolved organic matter from soil and
915 surface waters. *Aquatic Sciences*, *69*(1), 96–107.
916 https://doi.org/10.1007/s00027-006-0908-4
917 Kaiser, K., Benner, R., & Amon, R. M. W. (2017). The fate of terrigenous dissolved organic
918 carbon on the Eurasian shelves and export to the North Atlantic. *Journal of Geophysical*
919 *Research: Oceans*, *122*(1), 4–22. https://doi.org/10.1002/2016JC012380
920 Kaushal, N., Sanwlani, N., Tanzil, J. T. I., Cherukuru, N., Sahar, S., Müller, M., et al. (2021).
921 Coral Skeletal Luminescence Records Changes in Terrestrial Chromophoric Dissolved
922 Organic Matter in Tropical Coastal Waters. *Geophysical Research Letters*, *48*(8), 1–12.
923 https://doi.org/10.1029/2020GL092130
924 Kitidis, V., Shutler, J. D., Ashton, I., Warren, M., Brown, I., Findlay, H., et al. (2019). Winter
925 weather controls net influx of atmospheric CO2 on the north-west European shelf.
926 *Scientific Reports*, *9*(1), 1–11. https://doi.org/10.1038/s41598-019-56363-5
927 Koehler, B., Landelius, T., Weyhenmeyer, G. A., Machida, N., & Tranvik, L. J. (2014).

928 Sunlight-induced carbon dioxide emissions from inland waters. *Global Biogeochemical*
929 *Cycles*, *28*(7), 696–711. https://doi.org/10.1002/2014GB004850
930 Koehler, B., Broman, E., & Tranvik, L. J. (2016). Apparent quantum yield of photochemical
931 dissolved organic carbon mineralization in lakes. *Limnology and Oceanography*, *61*(6),
932 2207–2221. https://doi.org/10.1002/lno.10366
933 Koehler, B., Powers, L. C., Cory, R. M., Einarsdóttir, K., Gu, Y., Tranvik, L. J., et al. (2022).
934 Inter-laboratory differences in the apparent quantum yield for the photochemical
935 production of dissolved inorganic carbon in inland waters and implications for
936 photochemical rate modeling. *Limnology and Oceanography: Methods*, 320–337.
937 https://doi.org/10.1002/lom3.10489
938 Lee, Z. P., Du, K. P., & Arnone, R. (2005). A model for the diffuse attenuation coefficient of
939 downwelling irradiance. *Journal of Geophysical Research C: Oceans*, *110*(2), 1–10.
940 https://doi.org/10.1029/2004JC002275
941 Martin, P., Cherukuru, N., Tan, A. S. Y., Sanwlani, N., Mujahid, A., & Müller, M. (2018).
942 Distribution and cycling of terrigenous dissolved organic carbon in peatland-draining
943 rivers and coastal waters of Sarawak, Borneo. *Biogeosciences*, *15*(22), 6847–6865.
944 https://doi.org/10.5194/bg-15-6847-2018
945 Martin, P., Sanwlani, N., Lee, T., Wong, J., Chang, K., Wong, E., & Liew, S. (2021).
946 Dissolved organic matter from tropical peatlands reduces shelf sea light availability in
947 the Singapore Strait, Southeast Asia. *Marine Ecology Progress Series*.
948 https://doi.org/10.3354/meps13776

Martin, P., Moynihan, M. A., Chen, S., Woo, O. Y., Zhou, Y., Nichols, R. S., et al. (2022). Monsoon-driven biogeochemical dynamics in an equatorial shelf sea: Time-series observations in the Singapore Strait. *Estuarine, Coastal and Shelf Science*, *270*(April), 107855. https://doi.org/10.1016/j.ecss.2022.107855

Massicotte, P., Asmala, E., Stedmon, C., & Markager, S. (2017). Global distribution of dissolved organic matter along the aquatic continuum: Across rivers, lakes and oceans. *Science of The Total Environment*, *609*, 180–191. https://doi.org/10.1016/j.scitotenv.2017.07.076

Mathis, M., Logemann, K., Maerz, J., Lacroix, F., Hagemann, S., Chegini, F., et al. (2022). Seamless Integration of the Coastal Ocean in Global Marine Carbon Cycle Modeling. *Journal of Advances in Modeling Earth Systems*, *14*(8), 1–44. https://doi.org/10.1029/2021MS002789

Mayer, B., Stacke, T., Stottmeister, I., & Pohlmann, T. (2015). Sunda Shelf Seas: flushing rates and residence times. *Ocean Science Discussions*, *12*(3), 863–895. https://doi.org/10.5194/osd-12-863-2015

Mayer, B., Rixen, T., & Pohlmann, T. (2018). The spatial and temporal variability of air-sea CO2 fluxes and the effect of net coral reef calcification in the Indonesian Seas: A numerical sensitivity study. *Frontiers in Marine Science*, *5*(APR), 1–19. https://doi.org/10.3389/fmars.2018.00116

Miller, W. L., & Moran, M. A. (1997). Interaction of photochemical and microbial processes in the degradation of refractory dissolved organic matter from a coastal marine

970 environment. *Limnology and Oceanography*, *42*(6), 1317–1324.
971 https://doi.org/10.4319/lo.1997.42.6.1317
972 Moore, C. A., Farmer, C. T., & Zika, R. G. (1993). Influence of the Orinoco River on
973 hydrogen peroxide distribution and production in the eastern Caribbean. *Journal of*
974 *Geophysical Research: Oceans*, *98*(C2), 2289–2298. https://doi.org/10.1029/92JC02767
975 Moore, S., Gauci, V., Evans, C. D., & Page, S. E. (2011). Fluvial organic carbon losses from a
976 Bornean blackwater river. *Biogeosciences*, *8*(4), 901–909.
977 https://doi.org/10.5194/bg-8-901-2011
978 Mopper, K., Zhou, X., Kieber, R. J., Kieber, D. J., Sikorski, R. J., & Jones, R. D. (1991).
979 Photochemical degradation of dissolved organic carbon and its impact on the oceanic
980 carbon cycle. *Nature*, *353*(6339), 60–62. https://doi.org/10.1038/353060a0
981 Moran, M. A., & Zepp, R. G. (1997). Role of photoreactions in the formation of biologically
982 labile compounds from dissolved organic matter. *Limnology and Oceanography*, *42*(6),
983 1307–1316. https://doi.org/10.4319/lo.1997.42.6.1307
984 Moran, M. A., Sheldon, W. M., & Zepp, R. G. (2000). Carbon loss and optical property
985 changes during long-term photochemical and biological degradation of estuarine
986 dissolved organic matter. *Limnology and Oceanography*, *45*(6), 1254–1264.
987 https://doi.org/10.4319/lo.2000.45.6.1254
988 Müller, D., Warneke, T., Rixen, T., Müller, M., Jamahari, S., Denis, N., et al. (2015). Lateral
989 carbon fluxes and CO2 outgassing from a tropical peat-draining river. *Biogeosciences*,
990 *12*(20), 5967–5979. https://doi.org/10.5194/bg-12-5967-2015

991 Nichols, R. S., & Martin, P. (2021). Low biodegradability of dissolved organic matter from
992 Southeast Asian peat-draining rivers. *Journal of Geophysical Research: Biogeosciences*.
993 https://doi.org/10.1029/2020JG006182
994 Painter, S. C., Lapworth, D. J., Woodward, E. M. S., Kroeger, S., Evans, C. D., Mayor, D. J.,
995 & Sanders, R. J. (2018). Terrestrial dissolved organic matter distribution in the North
996 Sea. *Science of the Total Environment*, *630*, 630–647.
997 https://doi.org/10.1016/j.scitotenv.2018.02.237
998 Powers, L. C., & Miller, W. L. (2015). Photochemical production of CO and CO2 in the
999 Northern Gulf of Mexico: Estimates and challenges for quantifying the impact of
1000 photochemistry on carbon cycles. *Marine Chemistry*, *171*, 21–35.
1001 https://doi.org/10.1016/j.marchem.2015.02.004
1002 Powers, L. C., Brandes, J. A., Miller, W. L., & Stubbins, A. (2017). Using liquid
1003 chromatography-isotope ratio mass spectrometry to measure the δ13C of dissolved
1004 inorganic carbon photochemically produced from dissolved organic carbon. *Limnology*
1005 *and Oceanography: Methods*, *15*(1), 103–115. https://doi.org/10.1002/lom3.10146
1006 Rixen, T., Wit, F., Hutahaean, A. A., Schlüter, A., Baum, A., Klemme, A., et al. (2022). 4 -
1007 Carbon cycle in tropical peatlands and coastal seas. In T. C. Jennerjahn, T. Rixen, H. E.
1008 Irianto, & J. Samiaji (Eds.), *Science for the Protection of Indonesian Coastal*
1009 *Ecosystems (SPICE)* (pp. 83–142). Elsevier.
1010 https://doi.org/https://doi.org/10.1016/B978-0-12-815050-4.00011-0
1011 Semiletov, I., Pipko, I., Gustafsson, Ö., Anderson, L. G., Sergienko, V., Pugach, S., et al.

(2016). Acidification of East Siberian Arctic Shelf waters through addition of freshwater and terrestrial carbon. *Nature Geoscience*, *9*(5), 361–365. https://doi.org/10.1038/NEGO2695

Spencer, R. G. M., Stubbins, A., Hernes, P. J., Baker, A., Mopper, K., Aufdenkampe, A. K., et al. (2009). Photochemical degradation of dissolved organic matter and dissolved lignin phenols from the Congo River. *Journal of Geophysical Research*, *114*(G03010). https://doi.org/10.1029/2009JG000968

Stubbins, A., Spencer, R. G. M., Chen, H., Hatcher, P. G., Mopper, K., Hernes, P. J., et al. (2010). Illuminated darkness: Molecular signatures of Congo River dissolved organic matter and its photochemical alteration as revealed by ultrahigh precision mass spectrometry. *Limnology and Oceanography*, *55*(4), 1467–1477. https://doi.org/10.4319/lo.2010.55.4.1467

Stubbins, A., Mann, P. J., Powers, L., Bittar, T. B., Dittmar, T., McIntyre, C. P., et al. (2017). Low photolability of yedoma permafrost dissolved organic carbon. *Journal of Geophysical Research: Biogeosciences*, *122*(1), 200–211. https://doi.org/10.1002/2016JG003688

Susanto, D., Wei, Z., Adi, R., Zhang, Q., Fang, G., Fan, B., et al. (2016). Oceanography Surrounding Krakatau Volcano in the Sunda Strait, Indonesia. *Oceanography*, *29*(2), 0–29. https://doi.org/10.5670/oceanog.2016.31

Tzortziou, M., Osburn, C. L., & Neale, P. J. (2007). Photobleaching of dissolved organic material from a tidal marsh-estuarine system of the Chesapeake Bay. *Photochemistry*

and Photobiology, *83*(4), 782–792. https://doi.org/10.1111/j.1751-1097.2007.00142.x

Urtizberea, A., Dupont, N., Rosland, R., & Aksnes, D. L. (2013). Sensitivity of euphotic zone properties to CDOM variations in marine ecosystem models. *Ecological Modelling*, *256*, 16–22. https://doi.org/10.1016/j.ecolmodel.2013.02.010

Vähätalo, A. V., Salkinoja-Salonen, M., Taalas, P., & Salonen, K. (2000). Spectrum of the quantum yield for photochemical mineralization of dissolved organic carbon in a humic lake. *Limnology and Oceanography*, *45*(3), 664–676. https://doi.org/10.4319/lo.2000.45.3.0664

Vähätalo, A. V., Salonen, K., Münster, U., Järvinen, M., & Wetzel, R. G. (2003). Photochemical transformation of allochthonous organic matter provides bioavailable nutrients in a humic lake. *Archiv Fur Hydrobiologie*, *156*(3), 287–314. https://doi.org/10.1127/0003-9136/2003/0156-0287

Ward, C. P., Nalven, S. G., Crump, B. C., Kling, G. W., & Cory, R. M. (2017). Photochemical alteration of organic carbon draining permafrost soils shifts microbial metabolic pathways and stimulates respiration. *Nature Communications*, *8*(1), 1–7. https://doi.org/10.1038/s41467-017-00759-2

Ward, C. P., Bowen, J. C., Freeman, D. H., & Sharpless, C. M. (2021). Rapid and reproducible characterization of the wavelength dependence of aquatic photochemical reactions using light-emitting diodes. *Environmental Science and Technology Letters*, *8*(5), 437–442. https://doi.org/10.1021/acs.estlett.1c00172

Weishaar, J. L., Aiken, G. R., Bergamaschi, B. A., Fram, M. S., Fujii, R., & Mopper, K.

(2003). Evaluation of Specific Ultraviolet Absorbance as an Indicator of the Chemical Composition and Reactivity of Dissolved Organic Carbon. *Environmental Science & Technology*, *37*(20), 4702–4708. https://doi.org/10.1021/es030360x

White, E. M., Kieber, D. J., Sherrard, J., Miller, W. L., & Mopper, K. (2010). Carbon dioxide and carbon monoxide photoproduction quantum yields in the Delaware Estuary. *Marine Chemistry*, *118*(1–2), 11–21. https://doi.org/10.1016/j.marchem.2009.10.001

Wit, F., Rixen, T., Baum, A., Pranowo, W. S., & Hutahaean, A. A. (2018). The Invisible Carbon Footprint as a hidden impact of peatland degradation inducing marine carbonate dissolution in Sumatra, Indonesia. *Scientific Reports*, *8*(1), 17403. https://doi.org/10.1038/s41598-018-35769-7

Zepp, R. G. (2007). Solar UVR and aquatic Carbon, nitrogen, sulfur and metals cycles. In E. W. Helbling & H. Zagarese (Eds.) (pp. 137–184). Cambridge: Royal Society of Chemistry. https://doi.org/10.1039/9781847552266-00137

Zhou, Y., Martin, P., & Müller, M. (2019). Composition and cycling of dissolved organic matter from tropical peatlands of coastal Sarawak, Borneo, revealed by fluorescence spectroscopy and parallel factor analysis. *Biogeosciences*, *16*(13), 2733–2749. https://doi.org/10.5194/bg-16-2733-2019

Zhou, Y., Evans, C. D., Chen, Y., Chang, K. Y. W., & Martin, P. (2021). Extensive Remineralization of Peatland-Derived Dissolved Organic Carbon and Ocean Acidification in the Sunda Shelf Sea, Southeast Asia. *Journal of Geophysical Research: Oceans*, *126*(6), 1–23. https://doi.org/10.1029/2021JC017292

Zika, R. G. (1981). Chapter 10 Marine Organic Photochemistry. In *Elsevier Oceanography Series* (Vol. 31, pp. 299–325). https://doi.org/10.1016/S0422-9894(08)70332-5

Supporting Information

Photodegradation of dissolved organic carbon derived from tropical peatlands in the Sunda Shelf Sea, Southeast Asia

Yongli Zhou[1,*, †], Moritz Müller[2], Nagur Cherukuru[3], Patrick Martin[1,*]

[1]Asian School of the Environment, Nanyang Technological University, 639798 Singapore

[2]Faculty of Engineering, Computing and Science, Swinburne University of Science and Technology, 93350 Kuching, Sarawak, Malaysia

[3]CSIRO Oceans and Atmosphere Flagship, Canberra ACT 2601, Australia

[†]Current address: Ecosystem Center, Marine Biological Laboratory, Woods Hole, 02543, United States

A1 Apparent quantum yield (AQY) calculations

A1.1 Broadband AQY

The broadband apparent quantum yield ($\phi_{broadband}$) (unit: mol C (mol photons)$^{-1}$) for tDOC photo-remineralization was calculated for Exp 1–4 based on the DOC loss and the amount of photons absorbed following Fichot & Benner (2014) with the wavelength range modified:

$$\phi_{broadband} = \frac{DOC_{initial} - DOC_{final}}{\int_{t_0}^{t_{final}} \int_{290nm}^{700nm} \Xi((\lambda,t)\, d\lambda dt} \qquad \text{(S1)}$$

where DOC is the amount of DOC (mol) in the sample; $\Xi(\lambda, t)$ is the downwelling irradiance absorbed by CDOM in the quartz cell (mol photons nm^{-1} s^{-1}); λ denotes

wavelength (nm); t denotes time (s). $\Xi(\lambda, t)$ was calculated following Fichot & Benner (2014):

$$\Xi(\lambda, t) = E_d(\lambda)\, T\, S \left(1 - e^{-K_{d,cell}(\lambda,t)\, PL}\right) \frac{a_g(\lambda,t)}{K_{d,cell}(\lambda,t)} \quad \text{(S2)}$$

where $E_d(\lambda)$ is the downwelling irradiance spectrum of the xenon lamp just above the quartz cell (mol photons nm^{-1} s^{-1} m^{-2}, kept constant during the experiments); T (unitless) is the transmittance of the quartz window (0.95); S is the surface area (m^2) of the cuvette; and PL is the thickness (m) of the sample solution in the quartz cell. $K_{d,cell}(\lambda, t)$ is the diffuse attenuation coefficient of downwelling irradiance (m^{-1}) in the sample solution, which is the sum of the absorption of CDOM ($a_{CDOM}(\lambda, t)$) (m^{-1}), the absorption of water ($a_w(\lambda)$) (m^{-1}) and the backscattering of water ($bb_w(\lambda)$) (m^{-1}) following Fichot and Benner (2014):

$$K_{d,cell}(\lambda, t) \cong a_{CDOM}(\lambda, t) + a_w(\lambda) + bb_w(\lambda) \quad \text{(S3)}.$$

Because the samples were filtered, we did not include particulate absorption and backscattering here in the calculations. Note that the absorption of CDOM ($a_{CDOM}(\lambda, t)$) decreases over time due to photobleaching. It was measured at regular intervals during each experiment, and the mean absorption of every two consecutive time points was used to calculate the absorbed photons $\Xi(\lambda, t)$ for the corresponding time interval. $E_d(\lambda)$ was measured from 177 nm to 872 nm at 1 nm resolution with an Ocean Insights FLAME radiometer, and the spectrum between 290 nm and 318 nm was derived by linear interpolation assuming zero irradiance at ≤290 nm.

1131 **A1.2 Spectrally resolved AQY**

1132 The spectrally resolved AQY for tDOC photo-remineralization ($\phi_{DOC}(\lambda)$) was calculated for
1133 each experiment as in Aarnos et al. (2018). The $\phi_{DOC}(\lambda)$ was assumed to decrease
1134 exponentially with increasing wavelength (Gao & Zepp, 1998):

1135 $$\phi_{DOC}(\lambda) = c\, e^{-d\lambda} \quad \text{(S4)}$$

1136 where c (mol C (mol photons)$^{-1}$ nm^{-1}) and d (nm^{-1}) are positive constants. The amount of the
1137 photo-remineralized DOC can be related to the AQY spectrum $\phi_{DOC}(\lambda)$ and the absorbed
1138 irradiance $\Xi((\lambda, t)$:

1139 $$DOC_{initial} - DOC_{final} = \int_{t_{initial}}^{t_{final}} \int_{290nm}^{700nm} \phi_{DOC}(\lambda)\, \Xi((\lambda, t)\, d\lambda dt \quad \text{(S5)}.$$

1140 Therefore, c and d in Eq. 4 were iterated until the right side of Eq. S5 was as close as possible
1141 to the measured DOC loss, i.e., the left side of Eq. 5 using the *fminsearch* function of
1142 MATLAB. Because the optimized values of c and d are dependent on the starting values
1143 provided for iteration, a Monte Carlo approach was used to perturb the starting values and
1144 generate multiple combinations of c and d (Gu et al., 2017). The combination that provided
1145 the best fit between the modeled DOC loss and the measured DOC loss was selected (see
1146 Supporting Information in Aarnos et al., (2018)).

1147

1148 The concept of AQY was extended to the dose-dependent decrease in CDOM absorption. We
1149 refer to this as $\phi_{CDOM}(\lambda)$, which is the spectrally resolved AQY for the decrease in the
1150 volume-integrated CDOM absorption coefficient, with units of L m^{-1} (mol photons)$^{-1}$ nm^{-1}.
1151 For example, the decrease in the volume-integrated Napierian absorption coefficient at 350

nm (a_{350}) can be related to its spectrally resolved AQY $\phi_{a_{350}}(\lambda)$ and the absorbed irradiance $\Xi(\lambda, t)$ as:

$$\left(a_{350,initial} - - a_{350,final}\, V\right) = \int_{t_{initial}}^{t_{final}} \int_{290nm}^{700nm} \phi_{a_{350}}(\lambda)\, \Xi(\lambda, t)\, d\lambda dt \qquad \text{(S6)}$$

where V is the volume (in L) of the sample solution. To obtain the volume-integrated CDOM absorption, the measured absorption coefficient is multiplied by the volume of the water sample, yielding L m^{-1}. We assumed that, like $\phi_{DOC}(\lambda)$, the $\phi_a(\lambda)$ decreases exponentially with increasing wavelength. For a_{350}, we have:

$$\phi_{a_{350}}(\lambda) = c'\, e^{-d'\lambda} \qquad \text{(S7)}$$

where c' (L m^{-1} nm^{-1}) and d' (nm^{-1}) are positive constants, which were iterated until the right side of Eq. S6 was as close as possible to the left side of Eq. S6 using the *fminserach* function of MATLAB. This calculation was repeated across the CDOM absorption spectrum at 1-nm resolution from 250–700 nm, which returned 451 respective AQY spectra, i.e., AQY spectrum for a_{250}, AQY spectrum for a_{251}, AQY spectrum for a_{252}, …, AQY spectrum for a_{691}, AQY spectrum for a_{700}. Concatenating all these 1-dimensional AQY spectra returned the 2-dimensional AQY spectrum shown in Figure 4b.

A2 Photodegradation model

A2.1 Model calculations

The DOC concentration at time *T* was calculated from its value at time *T-1* and the amount of

DOC consumed during the period between *T-1* and *T* as:

$$DOC_T = DOC_{T-1} - \frac{\int_{T-1}^{T} pr_{DOC}(t)dt}{V} S \qquad \text{(S8)}$$

where $pr_{DOC}(t)$ is the areal rate of photo-remineralization of tDOC (mol C m^{-2} s^{-1}), *S* is the surface area of the water column under consideration (i.e., 1 m^2) and *V* is the volume of the water column (m^3), which was calculated from the water depth (Section 2.5.3) and surface area (1 m^2 here). The $pr_{DOC}(t)$ was calculated from the AQY spectrum ($\phi_{DOC}(\lambda)$) and the number of photons absorbed by CDOM ($\Xi(\lambda, t)$) in the water column:

$$pr_{DOC}(t) = \int_{300nm}^{700nm} \phi_{DOC}(\lambda)\, \Xi(\lambda, t)\, d\lambda \qquad \text{(S9).}$$

The irradiance absorbed by CDOM, $\Xi(\lambda, t)$, was calculated as:

$$\Xi(\lambda, t) = E_{o,0^-}(\lambda, t) \left(1 - e^{-K_o(\lambda,t)\, D}\right) f_{CDOM}(\lambda, t) \qquad \text{(S10)}$$

where $E_{o,0^-}(\lambda, t)$ is the total (i.e. upwelling + downwelling) scalar irradiance just below the water surface, $K_o(\lambda, t)$ is the diffuse attenuation coefficient of scalar irradiance, *D* is the water depth and $f_{CDOM}(\lambda, t)$ is the wavelength- and time-specific fraction of irradiance that is absorbed by CDOM. The right side of Eq. 10, except the term $f_{CDOM}(\lambda, t)$, calculates the total absorbed irradiance in the water column. We neglected the irradiance below 300 nm because the particulate absorption spectra, which were used for the calculation of K_o (see below), were not available below 300 nm. To assess the error caused by neglecting the irradiance below 300 nm, we used the simulated solar irradiance spectrum from 300–700 nm, and the AQY spectra for DOC photo-remineralization and CDOM photobleaching to back-calculate the DOC loss for our photodegradation Exp 1. The results only differed by 1.6% from the measured DOC loss, which shows that neglecting the irradiance below 300 nm only

1194 introduces a minimal error.

1195

1196 Because the upwelling irradiance is generally very small in waters that are optically deep,
1197 $E_{o,0^-}(\lambda,t)$ was approximated as the downwelling scalar irradiance, $E_{od,0^-}(\lambda,t)$, which was
1198 derived from the total (i.e. diffuse + direct) downwelling irradiance just above the water
1199 surface, $E_{d,0^+}(\lambda,t)$ (see Section 2.5.3), following (Fichot & Miller, 2010). $K_o\,(\lambda,t)$ was
1200 approximated using the diffuse attenuation coefficient of downwelling irradiance, $K_d\,(\lambda,t)$
1201 (Fichot & Miller, 2010). Therefore, Eq. 10 can be rewritten as Eq. 11 and was used in our
1202 model:

1203 $$\Xi(\lambda,t) = E_{od,0^-}(\lambda,t)\left(1 - e^{-K_d(\lambda,t)\,D}\right) f_{CDOM}(\lambda,t) \qquad \text{(S11)}.$$

1204

1205 Light attenuation $K_d\,(\lambda,t)$ was calculated following Lee et al. (2005):

1206 $$K_d(\lambda,t) = \left(1 + 0.005\,\theta(t)\right) a_{tot}(\lambda,t) + 1.48\left(1 - 0.52\,e^{-10.8\,a_{tot}(\lambda,t)}\right) b_{b\,tot}(\lambda) \qquad \text{(S12)}$$

1207 where $\theta(t)$ is the solar zenith angle above the water surface (degrees), $a_{tot}(\lambda,t)$ is the
1208 total absorption coefficient and $b_{b\,tot}(\lambda)$ is the total backscattering coefficient in the shelf
1209 waters:

1210 $$a_{tot}(\lambda,t) = a_{CDOM}\,(\lambda,t) + a_p\,(\lambda) + a_w\,(\lambda) \qquad \text{(S13)}$$

1211 $$b_{b\,tot}(\lambda) = b_{b_p}\,(\lambda) + b_{b_w}\,(\lambda) \qquad \text{(S14)}$$

1212 where the subscripts *CDOM, p, w* denote CDOM, particulates, and water, respectively.
1213 Particulate absorption and backscattering spectra were taken from in-situ measurements in
1214 our two model regions and were assumed to be constant over time.

The fraction of irradiance absorbed by CDOM, $f_{CDOM}(\lambda, t)$, was calculated as:

$$f_{CDOM}(\lambda, t) = \frac{(1+0.005\,\theta(t))\,a_{CDOM}(\lambda,t)}{K_d\,(\lambda,t)} \qquad \text{(S15)}$$

where the numerator is the diffuse attenuation coefficient of downwelling irradiance that is only caused by CDOM absorption, while the denominator is the actual K_d calculated from CDOM, particles, and water.

In Eq. S15, the CDOM spectrum at time point *T*, $a_{CDOM}(\lambda, T)$, can be calculated from the CDOM spectrum at time point *T-1* and the amount of CDOM that was photobleached between *T-1* and *T*. For example, for a_{350}:

$$a_{350,T} = a_{350,\ T-1} - \frac{\int_{T-1}^{T} pr_{a_{350}}(t)dt}{V} S \qquad \text{(S16)}$$

where $pr_{a_{350}}(t)$ is the areal rate of decrease in the volume-integrated a_{350}, *S* is the surface area of the water column (i.e., 1 m^2) and *V* is the volume of the water column. The $pr_{a_{350}}(t)$ was calculated as:

$$pr_{a_{350}}(t) = \int_{300nm}^{700nm} \phi_{a_{350}}(\lambda)\,\Xi(\lambda, t)\,d\lambda \qquad \text{(S17)}$$

where $\phi_{a_{350}}(\lambda)$ is the spectrally resolved AQY for the decrease in the volume-integrated a_{350} of CDOM (Eq. S7); $\Xi(\lambda, t)$ is the number of photons absorbed by CDOM (Eq. S11). Because $pr_{a_{350}}(t)$ needs to be calculated from $a_{350}(t)$, Eq. S16 cannot be solved. Thus, in practice, the $\int_{T-1}^{T} pr_{a_{350}}(t)\,dt$ in Eq. S16 was approximated as $pr_{a_{350},T-1}\Delta T$. Our results show that the daily change in CDOM absorption coefficient is small enough to allow this approximation. This calculation was applied across the CDOM spectrum at 1nm resolution

from 250–700 nm to obtain $a_{CDOM}(\lambda, t)$.

A2.2 Model input data

A2.2.1 Solar irradiance

The downwelling irradiance spectrum above the water surface, $E_{d,0^+}(\lambda, t)$, and the solar zenith angle, $\theta(t)$, for each time point were obtained from the Tropospheric Ultraviolet and Visible (TUV) Radiation Model (US National Center for Atmospheric Research, https://www2.acom.ucar.edu/modeling/tropospheric-ultraviolet-and-visible-tuv-radiation-model). Data were obtained on an hourly basis for the 15th day of each month of 2019 for two locations: 0.5°N 104.5°E, representative of the southern Malacca Strait, and 1.9°N 109.7°E, representative of the Talang Region. For both locations, $E_{d,0^+}(\lambda, t)$ under clear-sky and cloud-corrected conditions was obtained. The overhead ozone column, the optical depth of clouds, and the optical depth of aerosols as input parameters for the TUV model were obtained from NASA Earth Observations (https://neo.sci.gsfc.nasa.gov/).

A2.2.2 Particulate absorption and backscattering

For the southern Malacca Strait, particulate absorption and backscattering coefficients were obtained from bi-monthly measurements in the Singapore Strait between December 2018 to December 2020 (Martin et al., 2021). For the Talang Region, particulate absorption and

backscattering coefficients were measured in September 2017 at multiple stations between the estuary of the Samunsam River and the Talang Islands (Cherukuru et al., 2021). For both regions, the particulate absorption coefficients were measured on samples filtered onto glass fiber filters using an integrating sphere accessory on a spectrophotometer, while particulate backscattering coefficients were measured at 9 wavelengths using a Wetlabs BB9 lowered to 1m depth below water surface. Detailed methods can be found in Martin et al. (2021) and Cherukuru et al. (2021).

We fit a power-law function to each sample particulate backscattering spectrum (R^2 = 0.05–0.78 for the Southern Malacca Strait, samples with R^2 <0.34 were neglected; R^2 = 0.68–0.80 for Talang Region) to obtain spectra from 300–700 nm at 1-nm resolution. We calculated the mean and standard deviation of the particulate absorption and backscattering spectra as the model input parameters (i.e., $a_p(\lambda)$ and $b_{b_p}(\lambda)$).

A2.2.3 Starting values of DOC concentration and CDOM absorption

The initial DOC concentration for the southern Malacca Strait was calculated by assuming conservative mixing between peatland-draining rivers on Sumatra and seawater to a salinity of 29, which is approximately the lowest salinity in the Singapore Strait during the periods with strong terrestrial input (Zhou et al., 2021):

$$DOC(t_0) = DOC_{Sumatra} \times f_{river} \quad \text{(S18)}$$

where $DOC_{Sumatra}$ is the discharge-weighted average of riverine endmember DOC

concentration of the major rivers on Sumatra (890 μmol L^{-1}) (Wit et al., 2018), and f_{river} is the fraction of freshwater in the modeling regions. Note that a marine DOC component was not included in Eq. 18 because we only model the photodegradation of terrigenous DOC here. In addition, marine CDOM was found in very low concentration in these oligotrophic waters (Martin et al., 2021), so neglecting the marine CDOM does not affect our estimates of light absorption by CDOM.

The f_{river} was calculated from salinity:

$$f_{river} = (1 - \frac{sal_{mod}}{sal_{marine}}) \quad \text{(S19)}$$

where sal_{mod} is the salinity in the modeling region (i.e., 29) and sal_{marine} is the marine endmember salinity for the water from the open South China Sea, which is taken as 33 following Zhou et al. (2021). These calculations returned an initial DOC concentration of 108 μmol L^{-1} for the modeling for the Southern Malacca Strait.

CDOM spectral data from Sumatran rivers are not available. The DOC-specific absorbance at 254 nm ($SUVA_{254}$) of the Maludam River (5–6 L mg^{-1} m^{-1}) is comparable to that of other peatland-draining rivers in northwestern Borneo (Martin et al., 2018), and we take the CDOM-to-DOC ratio of the Maludam River as representative of peatland-draining rivers in Southeast Asia. Therefore, we calculated the initial CDOM spectrum for the Southern Malacca Strait based on the DOC-specific CDOM absorption spectrum of the Maludam River and our riverine end-member DOC concentration for Sumatra (890 μmol L^{-1}):

$$a_{CDOM,\ initial}(\lambda) = \frac{a_{CDOM,Maludam}(\lambda)}{DOC_{Maludam}} \times DOC_{Sumatra} \times f_{river} \quad \text{(S20)}$$

where $a_{CDOM,Maludam}(\lambda)$ and $DOC_{Maludam}$ is the CDOM spectrum and DOC concentration, respectively, of the Maludam River water sample (collected in December 2017). The starting CDOM absorption spectrum in Day 1 for modeling is shown in Fig. S3e.

For the Talang Region, the starting DOC concentration and the CDOM absorption spectrum in Day 1 were calculated by assuming conservative mixing between the Samunsam River water and seawater to salinity of 29 using Eqns. S18–S20. Riverine endmember DOC concentration and CDOM absorption in the Samunsam River were measured in March and September 2017 (Martin et al., 2018). Calculations using the annual mean riverine DOC concentration of 1493 μmol L^{-1} returned an initial DOC concentration of 181 μmol L^{-1} and an initial CDOM absorption spectrum (Fig. S3f) for modeling for the Talang Region.

A2.3 Photochemical decay constant of UniDOM

First, we calculated the depth-normalized photochemical decay constant, $\emptyset$, based on the monthly loss of DOC of year 1 from our modeling results under the cloud-corrected conditions:

$$\emptyset = \frac{\ln(DOC_{t1}) - \ln(DOC_{t2})}{\Delta t} \quad \text{(S21)}$$

where DOC_{t1} and DOC_{t2} is the DOC concentration in the first and the last day of the month, respectively. We then converted the $\emptyset$ to $\emptyset^{ref}$ based on equations in Anderson et al. (2019):

$$\emptyset^{ref} = \frac{\emptyset \times D}{\frac{1}{k_{UV}} - \frac{e^{-k_{UV}\,D}}{k_{UV}}} \qquad \text{(S22)}$$

where D is the water depth and k_{UV} is the extinction coefficient, which was approximated using the water UV attenuation, k_{UVw}, (0.12 m^{-1}) and CDOM decadic absorption coefficient at 350nm, k_{350}:

$$k_{UV} = k_{UVw} + k_{350} \qquad \text{(S23).}$$

This returned $\emptyset^{ref}$ for each month and we report the mean value to account for the seasonal variation in solar irradiance. A decline in the decay constant with age proposed by Anderson et al. (2019) was not considered in our calculation because we did not observe a decrease in the apparent quantum yield over the course of our photodegradation experiments (Table S4).

References in Supporting information

Aarnos, H., Ylöstalo, P., & Vähätalo, A. V. (2012). Seasonal phototransformation of dissolved organic matter to ammonium, dissolved inorganic carbon, and labile substrates supporting bacterial biomass across the Baltic Sea. *Journal of Geophysical Research: Biogeosciences*, *117*(1), 1–14. https://doi.org/10.1029/2010JG001633

Aarnos, H., Gélinas, Y., Kasurinen, V., Gu, Y., Puupponen, V. M., & Vähätalo, A. V. (2018). Photochemical Mineralization of Terrigenous DOC to Dissolved Inorganic Carbon in Ocean. *Global Biogeochemical Cycles*, *32*(2), 250–266. https://doi.org/10.1002/2017GB005698

Aksnes, D. L., Dupont, N., Staby, A., Fiksen, Ø., Kaartvedt, S., & Aure, J. (2009). Coastal

water darkening and implications for mesopelagic regime shifts in Norwegian fjords. *Marine Ecology Progress Series*, *387*(Jerlov 1968), 39–49. https://doi.org/10.3354/meps08120

Alkhatib, M., Jennerjahn, T. C., & Samiaji, J. (2007). Biogeochemistry of the Dumai River estuary, Sumatra, Indonesia, a tropical black-water river. *Limnology and Oceanography*, *52*(6), 2410–2417. https://doi.org/10.4319/lo.2007.52.6.2410

Allesson, L., Koehler, B., Thrane, J. E., Andersen, T., & Hessen, D. O. (2021). The role of photomineralization for CO2 emissions in boreal lakes along a gradient of dissolved organic matter. *Limnology and Oceanography*, *66*(1), 158–170. https://doi.org/10.1002/lno.11594

Anderson, T. R., Rowe, E. C., Polimene, L., Tipping, E., Evans, C. D., Barry, C. D. G., et al. (2019). Unified concepts for understanding and modelling turnover of dissolved organic matter from freshwaters to the ocean: the UniDOM model. *Biogeochemistry*, *146*(2), 105–123. https://doi.org/10.1007/s10533-019-00621-1

Apell, J. N., & McNeill, K. (2019). Updated and validated solar irradiance reference spectra for estimating environmental photodegradation rates. *Environmental Science: Processes and Impacts*, *21*(3), 427–437. https://doi.org/10.1039/c8em00478a

Baum, A., Rixen, T., & Samiaji, J. (2007). Relevance of peat draining rivers in central Sumatra for the riverine input of dissolved organic carbon into the ocean. *Estuarine, Coastal and Shelf Science*, *73*(3–4), 563–570. https://doi.org/10.1016/j.ecss.2007.02.012

Beleites, C., & Sergo, V. (2012). hyperSpec: a package to handle hyperspectral data sets in R.

Journal of Statistical Software.

Cai, W.-J. (2011). Estuarine and Coastal Ocean Carbon Paradox: CO 2 Sinks or Sites of Terrestrial Carbon Incineration? *Annual Review of Marine Science*, *3*(1), 123–145. https://doi.org/10.1146/annurev-marine-120709-142723

Catalán, N., Marcé, R., Kothawala, D. N., & Tranvik, L. J. (2016). Organic carbon decomposition rates controlled by water retention time across inland waters. *Nature Geoscience*, *9*(7), 501–504. https://doi.org/10.1038/ngeo2720

Chen, H., Abdulla, H. A. N., Sanders, R. L., Myneni, S. C. B., Mopper, K., & Hatcher, P. G. (2014). Production of Black Carbon-like and Aliphatic Molecules from Terrestrial Dissolved Organic Matter in the Presence of Sunlight and Iron. *Environmental Science and Technology Letters*, *1*(10), 399–404. https://doi.org/10.1021/ez5002598

Cherukuru, N., Martin, P., Sanwlani, N., Mujahid, A., & Müller, M. (2021). A semi-analytical optical remote sensing model to estimate suspended sediment and dissolved organic carbon in tropical coastal waters influenced by peatland-draining river discharges off sarawak, borneo. *Remote Sensing*, *13*(1), 1–31. https://doi.org/10.3390/rs13010099

Ciais, P., Sabine, C., & Bala, G. (2013). Chapter 6: Carbon and other biogeochemical cycles. *Climate Change 2013: The Physical Science Basis*.

Cory, R. M., & Kling, G. W. (2018). Interactions between sunlight and microorganisms influence dissolved organic matter degradation along the aquatic continuum. *Limnology and Oceanography Letters*, *3*(3), 102–116. https://doi.org/10.1002/lol2.10060

Cory, R. M., McKnight, D. M., Chin, Y. P., Miller, P., & Jaros, C. L. (2007). Chemical

characteristics of fulvic acids from Arctic surface waters: Microbial contributions and photochemical transformations. *Journal of Geophysical Research: Biogeosciences*, *112*(4), 1–14. https://doi.org/10.1029/2006JG000343

Dittmar, T., Whitehead, K., Minor, E. C., & Koch, B. P. (2007). Tracing terrigenous dissolved organic matter and its photochemical decay in the ocean by using liquid chromatography/mass spectrometry. *Marine Chemistry*, *107*(3), 378–387. https://doi.org/10.1016/j.marchem.2007.04.006

Evans, C. D., Futter, M. N., Moldan, F., Valinia, S., Frogbrook, Z., & Kothawala, D. N. (2017). Variability in organic carbon reactivity across lake residence time and trophic gradients. *Nature Geoscience*, *10*(11), 832–835. https://doi.org/10.1038/NGEO3051

Fichot, C. G., & Benner, R. (2014). The fate of terrigenous dissolved organic carbon in a river-influenced ocean margin. *Global Biogeochemical Cycles*, *28*(3), 300–318. https://doi.org/10.1002/2013GB004670

Fichot, C. G., & Miller, W. L. (2010). An approach to quantify depth-resolved marine photochemical fluxes using remote sensing: Application to carbon monoxide (CO) photoproduction. *Remote Sensing of Environment*, *114*(7), 1363–1377. https://doi.org/10.1016/j.rse.2010.01.019

Gao, H., & Zepp, R. G. (1998). Factors influencing photoreactions of dissolved organic matter in a coastal river of the southeastern United States. *Environmental Science and Technology*, *32*(19), 2940–2946. https://doi.org/10.1021/es9803660

GEBCO Compilation Group. (2020). GEBCO 2020 Grid.

https://doi.org/10.5285/a29c5465-b138-234d-e053-6c86abc040b9

Giesen, W., Wijedasa, L. S., & Page, S. E. (2018). Unique Southeast Asian peat swamp forest habitats have relatively few distinctive plant species. *Mires and Peat*, *22*, 1–13. https://doi.org/10.19189/MaP.2017.OMB.287

Gu, Y., Lensu, A., Perämäki, S., Ojala, A., & Vähätalo, A. V. (2017). Iron and pH Regulating the Photochemical Mineralization of Dissolved Organic Carbon. *ACS Omega*, *2*(5), 1905–1914. https://doi.org/10.1021/acsomega.7b00453

Helms, J. R., Stubbins, A., Ritchie, J. D., Minor, E. C., Kieber, D. J., & Mopper, K. (2008). Absorption spectral slopes and slope ratios as indicators of molecular weight, source, and photobleaching of chromophoric dissolved organic matter. *Limnology and Oceanography*, *53*(3), 955–969. https://doi.org/10.4319/lo.2008.53.3.0955

Helms, J. R., Stubbins, A., Perdue, E. M., Green, N. W., Chen, H., & Mopper, K. (2013). Photochemical bleaching of oceanic dissolved organic matter and its effect on absorption spectral slope and fluorescence. *Marine Chemistry*, *155*, 81–91. https://doi.org/10.1016/j.marchem.2013.05.015

Helms, J. R., Mao, J., Schmidt-Rohr, K., Abdulla, H., & Mopper, K. (2013). Photochemical flocculation of terrestrial dissolved organic matter and iron. *Geochimica et Cosmochimica Acta*, *121*, 398–413. https://doi.org/10.1016/j.gca.2013.07.025

Jankowski, J. J., Kieber, D. J., & Mopper, K. (1999a). Nitrate and nitrite ultraviolet actinometers. *Photochemistry and Photobiology*, *70*(3), 319–328. https://doi.org/10.1111/j.1751-1097.1999.tb08143.x

1425 Jankowski, J. J., Kieber, D. J., & Mopper, K. (1999b). Nitrate and Nitrite Ultraviolet
1426 Actinometers. *Photochemistry and Photobiology*, *70*(3), 319–328.
1427 https://doi.org/10.1111/j.1751-1097.1999.tb08143.x
1428 Johannessen, S. C., & Miller, W. L. (2001). Quantum yield for the photochemical production
1429 of dissolved inorganic carbon in seawater. *Marine Chemistry*, *76*(4), 271–283.
1430 https://doi.org/10.1016/S0304-4203(01)00067-6
1431 Judd, K. E., Crump, B. C., & Kling, G. W. (2007). Bacterial responses in activity and
1432 community composition to photo-oxidation of dissolved organic matter from soil and
1433 surface waters. *Aquatic Sciences*, *69*(1), 96–107.
1434 https://doi.org/10.1007/s00027-006-0908-4
1435 Kaiser, K., Benner, R., & Amon, R. M. W. (2017). The fate of terrigenous dissolved organic
1436 carbon on the Eurasian shelves and export to the North Atlantic. *Journal of Geophysical*
1437 *Research: Oceans*, *122*(1), 4–22. https://doi.org/10.1002/2016JC012380
1438 Kaushal, N., Sanwlani, N., Tanzil, J. T. I., Cherukuru, N., Sahar, S., Müller, M., et al. (2021).
1439 Coral Skeletal Luminescence Records Changes in Terrestrial Chromophoric Dissolved
1440 Organic Matter in Tropical Coastal Waters. *Geophysical Research Letters*, *48*(8), 1–12.
1441 https://doi.org/10.1029/2020GL092130
1442 Kitidis, V., Shutler, J. D., Ashton, I., Warren, M., Brown, I., Findlay, H., et al. (2019). Winter
1443 weather controls net influx of atmospheric CO2 on the north-west European shelf.
1444 *Scientific Reports*, *9*(1), 1–11. https://doi.org/10.1038/s41598-019-56363-5
1445 Koehler, B., Landelius, T., Weyhenmeyer, G. A., Machida, N., & Tranvik, L. J. (2014).

Sunlight-induced carbon dioxide emissions from inland waters. *Global Biogeochemical Cycles*, *28*(7), 696–711. https://doi.org/10.1002/2014GB004850

Koehler, B., Broman, E., & Tranvik, L. J. (2016). Apparent quantum yield of photochemical dissolved organic carbon mineralization in lakes. *Limnology and Oceanography*, *61*(6), 2207–2221. https://doi.org/10.1002/lno.10366

Koehler, B., Powers, L. C., Cory, R. M., Einarsdóttir, K., Gu, Y., Tranvik, L. J., et al. (2022). Inter-laboratory differences in the apparent quantum yield for the photochemical production of dissolved inorganic carbon in inland waters and implications for photochemical rate modeling. *Limnology and Oceanography: Methods*, 320–337. https://doi.org/10.1002/lom3.10489

Lee, Z. P., Du, K. P., & Arnone, R. (2005). A model for the diffuse attenuation coefficient of downwelling irradiance. *Journal of Geophysical Research C: Oceans*, *110*(2), 1–10. https://doi.org/10.1029/2004JC002275

Martin, P., Cherukuru, N., Tan, A. S. Y., Sanwlani, N., Mujahid, A., & Müller, M. (2018). Distribution and cycling of terrigenous dissolved organic carbon in peatland-draining rivers and coastal waters of Sarawak, Borneo. *Biogeosciences*, *15*(22), 6847–6865. https://doi.org/10.5194/bg-15-6847-2018

Martin, P., Sanwlani, N., Lee, T., Wong, J., Chang, K., Wong, E., & Liew, S. (2021). Dissolved organic matter from tropical peatlands reduces shelf sea light availability in the Singapore Strait, Southeast Asia. *Marine Ecology Progress Series*. https://doi.org/10.3354/meps13776

1467 Martin, P., Moynihan, M. A., Chen, S., Woo, O. Y., Zhou, Y., Nichols, R. S., et al. (2022).
1468 Monsoon-driven biogeochemical dynamics in an equatorial shelf sea: Time-series
1469 observations in the Singapore Strait. *Estuarine, Coastal and Shelf Science*, *270*(April),
1470 107855. https://doi.org/10.1016/j.ecss.2022.107855
1471 Massicotte, P., Asmala, E., Stedmon, C., & Markager, S. (2017). Global distribution of
1472 dissolved organic matter along the aquatic continuum: Across rivers, lakes and oceans.
1473 *Science of The Total Environment*, *609*, 180–191.
1474 https://doi.org/10.1016/j.scitotenv.2017.07.076
1475 Mathis, M., Logemann, K., Maerz, J., Lacroix, F., Hagemann, S., Chegini, F., et al. (2022).
1476 Seamless Integration of the Coastal Ocean in Global Marine Carbon Cycle Modeling.
1477 *Journal of Advances in Modeling Earth Systems*, *14*(8), 1–44.
1478 https://doi.org/10.1029/2021MS002789
1479 Mayer, B., Stacke, T., Stottmeister, I., & Pohlmann, T. (2015). Sunda Shelf Seas: flushing
1480 rates and residence times. *Ocean Science Discussions*, *12*(3), 863–895.
1481 https://doi.org/10.5194/osd-12-863-2015
1482 Mayer, B., Rixen, T., & Pohlmann, T. (2018). The spatial and temporal variability of air-sea
1483 CO2 fluxes and the effect of net coral reef calcification in the Indonesian Seas: A
1484 numerical sensitivity study. *Frontiers in Marine Science*, *5*(APR), 1–19.
1485 https://doi.org/10.3389/fmars.2018.00116
1486 Miller, W. L., & Moran, M. A. (1997). Interaction of photochemical and microbial processes
1487 in the degradation of refractory dissolved organic matter from a coastal marine

environment. *Limnology and Oceanography*, *42*(6), 1317–1324. https://doi.org/10.4319/lo.1997.42.6.1317

Moore, C. A., Farmer, C. T., & Zika, R. G. (1993). Influence of the Orinoco River on hydrogen peroxide distribution and production in the eastern Caribbean. *Journal of Geophysical Research: Oceans*, *98*(C2), 2289–2298. https://doi.org/10.1029/92JC02767

Moore, S., Gauci, V., Evans, C. D., & Page, S. E. (2011). Fluvial organic carbon losses from a Bornean blackwater river. *Biogeosciences*, *8*(4), 901–909. https://doi.org/10.5194/bg-8-901-2011

Mopper, K., Zhou, X., Kieber, R. J., Kieber, D. J., Sikorski, R. J., & Jones, R. D. (1991). Photochemical degradation of dissolved organic carbon and its impact on the oceanic carbon cycle. *Nature*, *353*(6339), 60–62. https://doi.org/10.1038/353060a0

Moran, M. A., & Zepp, R. G. (1997). Role of photoreactions in the formation of biologically labile compounds from dissolved organic matter. *Limnology and Oceanography*, *42*(6), 1307–1316. https://doi.org/10.4319/lo.1997.42.6.1307

Moran, M. A., Sheldon, W. M., & Zepp, R. G. (2000). Carbon loss and optical property changes during long-term photochemical and biological degradation of estuarine dissolved organic matter. *Limnology and Oceanography*, *45*(6), 1254–1264. https://doi.org/10.4319/lo.2000.45.6.1254

Müller, D., Warneke, T., Rixen, T., Müller, M., Jamahari, S., Denis, N., et al. (2015). Lateral carbon fluxes and CO2 outgassing from a tropical peat-draining river. *Biogeosciences*, *12*(20), 5967–5979. https://doi.org/10.5194/bg-12-5967-2015

1509 Nichols, R. S., & Martin, P. (2021). Low biodegradability of dissolved organic matter from
1510 Southeast Asian peat-draining rivers. *Journal of Geophysical Research: Biogeosciences*.
1511 https://doi.org/10.1029/2020JG006182
1512 Painter, S. C., Lapworth, D. J., Woodward, E. M. S., Kroeger, S., Evans, C. D., Mayor, D. J.,
1513 & Sanders, R. J. (2018). Terrestrial dissolved organic matter distribution in the North
1514 Sea. *Science of the Total Environment*, *630*, 630–647.
1515 https://doi.org/10.1016/j.scitotenv.2018.02.237
1516 Powers, L. C., & Miller, W. L. (2015). Photochemical production of CO and CO2 in the
1517 Northern Gulf of Mexico: Estimates and challenges for quantifying the impact of
1518 photochemistry on carbon cycles. *Marine Chemistry*, *171*, 21–35.
1519 https://doi.org/10.1016/j.marchem.2015.02.004
1520 Powers, L. C., Brandes, J. A., Miller, W. L., & Stubbins, A. (2017). Using liquid
1521 chromatography-isotope ratio mass spectrometry to measure the δ13C of dissolved
1522 inorganic carbon photochemically produced from dissolved organic carbon. *Limnology*
1523 *and Oceanography: Methods*, *15*(1), 103–115. https://doi.org/10.1002/lom3.10146
1524 Rixen, T., Wit, F., Hutahaean, A. A., Schlüter, A., Baum, A., Klemme, A., et al. (2022). 4 -
1525 Carbon cycle in tropical peatlands and coastal seas. In T. C. Jennerjahn, T. Rixen, H. E.
1526 Irianto, & J. Samiaji (Eds.), *Science for the Protection of Indonesian Coastal*
1527 *Ecosystems (SPICE)* (pp. 83–142). Elsevier.
1528 https://doi.org/https://doi.org/10.1016/B978-0-12-815050-4.00011-0
1529 Semiletov, I., Pipko, I., Gustafsson, Ö., Anderson, L. G., Sergienko, V., Pugach, S., et al.

(2016). Acidification of East Siberian Arctic Shelf waters through addition of freshwater and terrestrial carbon. *Nature Geoscience*, *9*(5), 361–365. https://doi.org/10.1038/NEGO2695

Spencer, R. G. M., Stubbins, A., Hernes, P. J., Baker, A., Mopper, K., Aufdenkampe, A. K., et al. (2009). Photochemical degradation of dissolved organic matter and dissolved lignin phenols from the Congo River. *Journal of Geophysical Research*, *114*(G03010). https://doi.org/10.1029/2009JG000968

Stubbins, A., Spencer, R. G. M., Chen, H., Hatcher, P. G., Mopper, K., Hernes, P. J., et al. (2010). Illuminated darkness: Molecular signatures of Congo River dissolved organic matter and its photochemical alteration as revealed by ultrahigh precision mass spectrometry. *Limnology and Oceanography*, *55*(4), 1467–1477. https://doi.org/10.4319/lo.2010.55.4.1467

Stubbins, A., Mann, P. J., Powers, L., Bittar, T. B., Dittmar, T., McIntyre, C. P., et al. (2017). Low photolability of yedoma permafrost dissolved organic carbon. *Journal of Geophysical Research: Biogeosciences*, *122*(1), 200–211. https://doi.org/10.1002/2016JG003688

Susanto, D., Wei, Z., Adi, R., Zhang, Q., Fang, G., Fan, B., et al. (2016). Oceanography Surrounding Krakatau Volcano in the Sunda Strait, Indonesia. *Oceanography*, *29*(2), 0–29. https://doi.org/10.5670/oceanog.2016.31

Tzortziou, M., Osburn, C. L., & Neale, P. J. (2007). Photobleaching of dissolved organic material from a tidal marsh-estuarine system of the Chesapeake Bay. *Photochemistry*

and Photobiology, *83*(4), 782–792. https://doi.org/10.1111/j.1751-1097.2007.00142.x

Urtizberea, A., Dupont, N., Rosland, R., & Aksnes, D. L. (2013). Sensitivity of euphotic zone properties to CDOM variations in marine ecosystem models. *Ecological Modelling*, *256*, 16–22. https://doi.org/10.1016/j.ecolmodel.2013.02.010

Vähätalo, A. V., Salkinoja-Salonen, M., Taalas, P., & Salonen, K. (2000). Spectrum of the quantum yield for photochemical mineralization of dissolved organic carbon in a humic lake. *Limnology and Oceanography*, *45*(3), 664–676. https://doi.org/10.4319/lo.2000.45.3.0664

Vähätalo, A. V., Salonen, K., Münster, U., Järvinen, M., & Wetzel, R. G. (2003). Photochemical transformation of allochthonous organic matter provides bioavailable nutrients in a humic lake. *Archiv Fur Hydrobiologie*, *156*(3), 287–314. https://doi.org/10.1127/0003-9136/2003/0156-0287

Ward, C. P., Nalven, S. G., Crump, B. C., Kling, G. W., & Cory, R. M. (2017). Photochemical alteration of organic carbon draining permafrost soils shifts microbial metabolic pathways and stimulates respiration. *Nature Communications*, *8*(1), 1–7. https://doi.org/10.1038/s41467-017-00759-2

Ward, C. P., Bowen, J. C., Freeman, D. H., & Sharpless, C. M. (2021). Rapid and reproducible characterization of the wavelength dependence of aquatic photochemical reactions using light-emitting diodes. *Environmental Science and Technology Letters*, *8*(5), 437–442. https://doi.org/10.1021/acs.estlett.1c00172

Weishaar, J. L., Aiken, G. R., Bergamaschi, B. A., Fram, M. S., Fujii, R., & Mopper, K.

(2003). Evaluation of Specific Ultraviolet Absorbance as an Indicator of the Chemical Composition and Reactivity of Dissolved Organic Carbon. *Environmental Science & Technology*, *37*(20), 4702–4708. https://doi.org/10.1021/es030360x

White, E. M., Kieber, D. J., Sherrard, J., Miller, W. L., & Mopper, K. (2010). Carbon dioxide and carbon monoxide photoproduction quantum yields in the Delaware Estuary. *Marine Chemistry*, *118*(1–2), 11–21. https://doi.org/10.1016/j.marchem.2009.10.001

Wit, F., Rixen, T., Baum, A., Pranowo, W. S., & Hutahaean, A. A. (2018). The Invisible Carbon Footprint as a hidden impact of peatland degradation inducing marine carbonate dissolution in Sumatra, Indonesia. *Scientific Reports*, *8*(1), 17403. https://doi.org/10.1038/s41598-018-35769-7

Zepp, R. G. (2007). Solar UVR and aquatic Carbon, nitrogen, sulfur and metals cycles. In E. W. Helbling & H. Zagarese (Eds.) (pp. 137–184). Cambridge: Royal Society of Chemistry. https://doi.org/10.1039/9781847552266-00137

Zhou, Y., Martin, P., & Müller, M. (2019). Composition and cycling of dissolved organic matter from tropical peatlands of coastal Sarawak, Borneo, revealed by fluorescence spectroscopy and parallel factor analysis. *Biogeosciences*, *16*(13), 2733–2749. https://doi.org/10.5194/bg-16-2733-2019

Zhou, Y., Evans, C. D., Chen, Y., Chang, K. Y. W., & Martin, P. (2021). Extensive Remineralization of Peatland-Derived Dissolved Organic Carbon and Ocean Acidification in the Sunda Shelf Sea, Southeast Asia. *Journal of Geophysical Research: Oceans*, *126*(6), 1–23. https://doi.org/10.1029/2021JC017292

1593 Zika, R. G. (1981). Chapter 10 Marine Organic Photochemistry. In *Elsevier Oceanography*
1594 *Series* (Vol. 31, pp. 299–325). https://doi.org/10.1016/S0422-9894(08)70332-5
1595
1596
1597
1598
1599

A3 Supplementary Figures and Tables

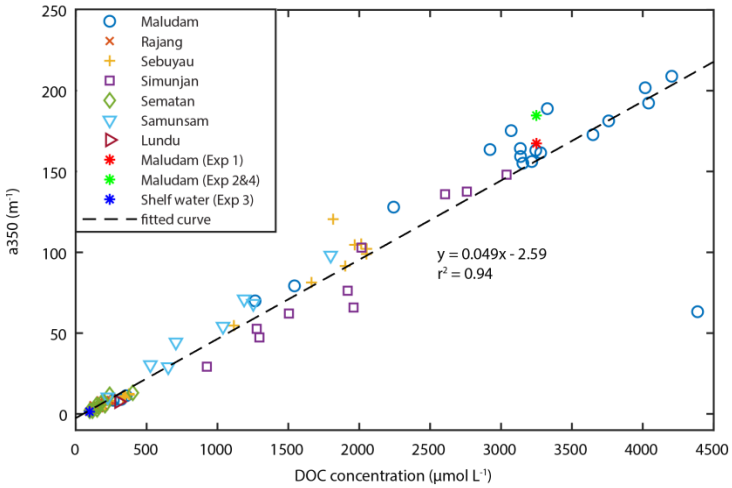

Figure S1. Relationship between DOC concentration and CDOM absorption (a_{350}) across different rivers in Sarawak, Borneo (data from Martin et al. 2018), and in the shelf sea water sample collected in the Singapore Strait for Exp 3. Samples used to determine tDOC AQY in this study follow the relationship.

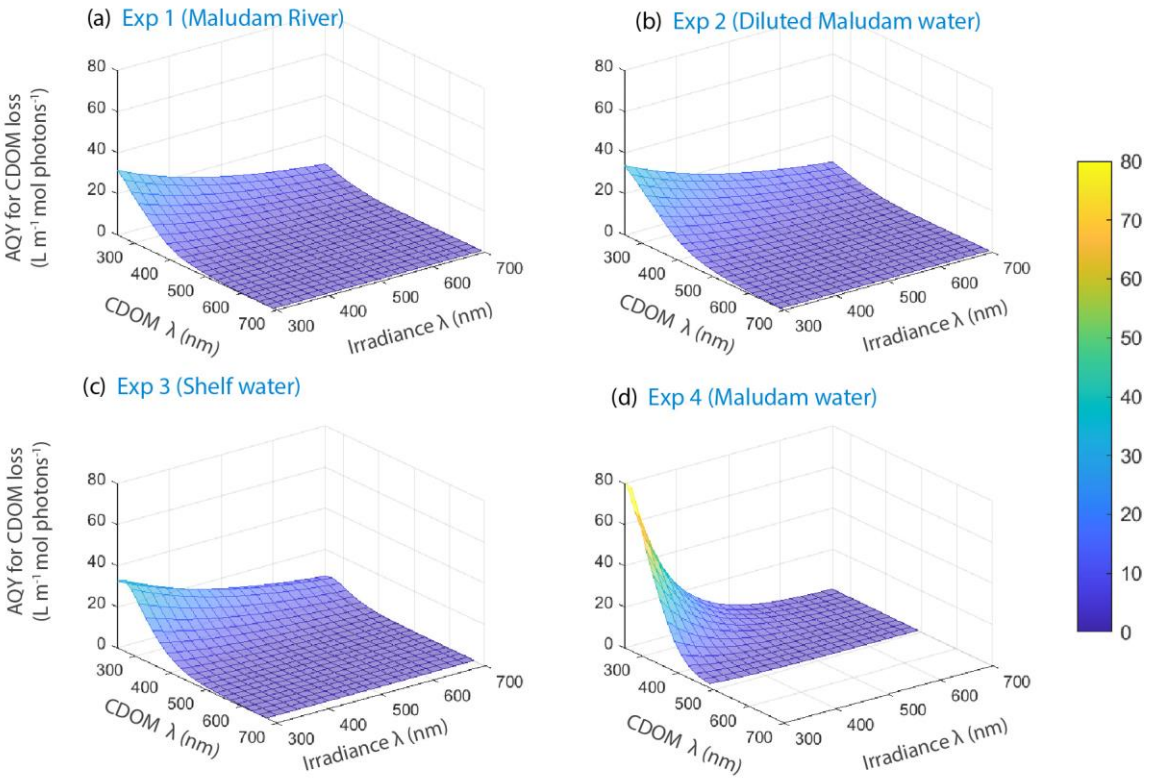

Figure S2. Photochemical efficiency spectra for CDOM photobleaching, i.e. decrease in volume-integrated absorption coefficient, calculated from data of Exp 1–4. In Exp 4, the AQY for CDOM photobleaching above 500 nm of the CDOM absorption spectrum were given in negative values, due to the measurement noise of CDOM absorption at the longer wavelengths, and thus omitted.

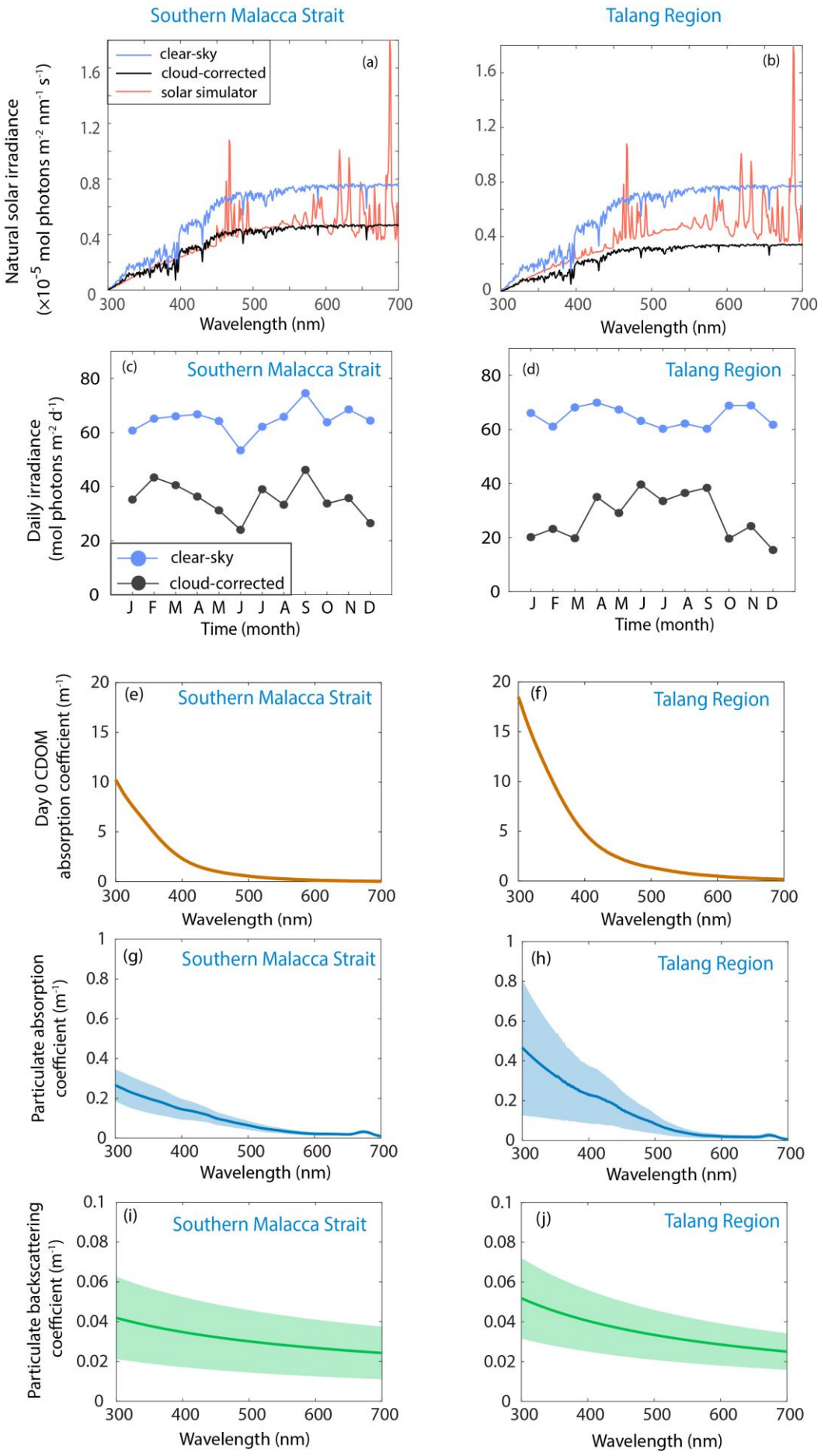
Southern Malacca Strait
Talang Region
clear-sky
cloud-corrected
solar simulator
(a)
(b)
Natural solar irradiance
(×10-5 mol photons m-2 nm-1 s-1)
Wavelength (nm)
(c)
(d)
Daily irradiance
(mol photons m-2 d-1)
J F M A M J J A S O N D
Time (month)
(e)
(f)
Day 0 CDOM
absorption coefficient (m-1)
(g)
(h)
Particulate absorption
coefficient (m-1)
(i)
(j)
Particulate backscattering
coefficient (m-1)

1617

Figure S3. Model input data for both modeling regions. (a) – (b) Annual mean noon-time (12 pm local time) natural solar irradiance under clear-sky and cloud-corrected conditions for both modeling regions, compared with the irradiance of the solar simulator for Exp 1–4. (c)–(d) Seasonal variations in the daily irradiance under clear-sky and cloud-corrected conditions. Daily irradiance for each month was integrated over 300 to 700 nm and 24 hours. (e)–(f) Initial CDOM absorption spectra (i.e. in Day 0). (g)–(h) Particulate absorption spectrum. (i)–(j) Particulate backscattering spectrum. The shading in panels g–j indicates the uncertainties of the spectra calculated from all the spectrum for estimating the model output by Monte Carlo simulation.

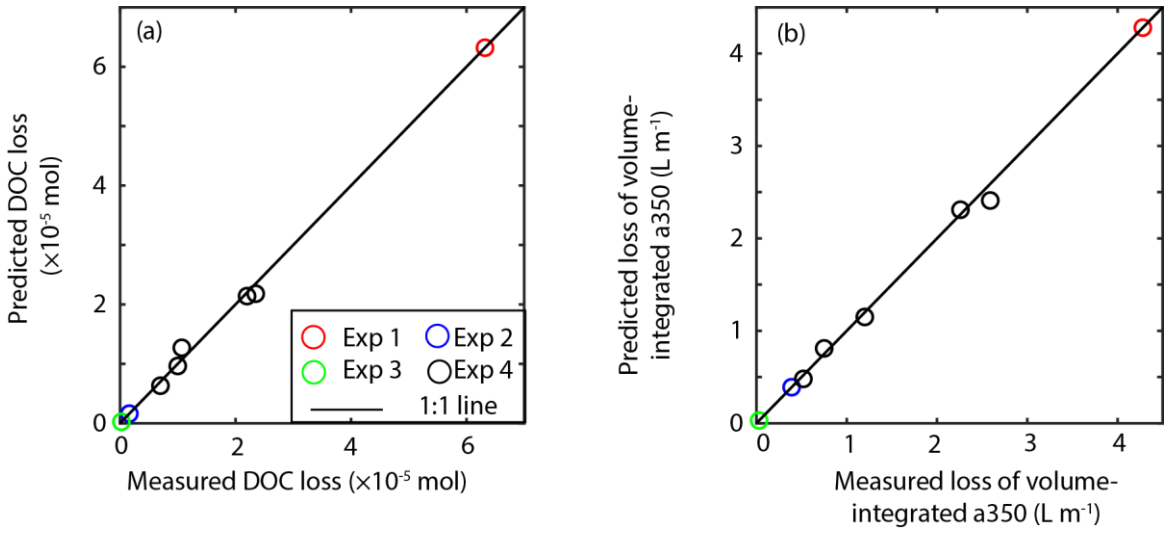

Figure S4. Comparison of the measured and the optimized AQY-predicted (a) loss of DOC and (b) loss of the volume-integrated a_{350} of CDOM of Exp 1 – 4. Data of Exp 4 were from the multiple cut-off filters treatments.

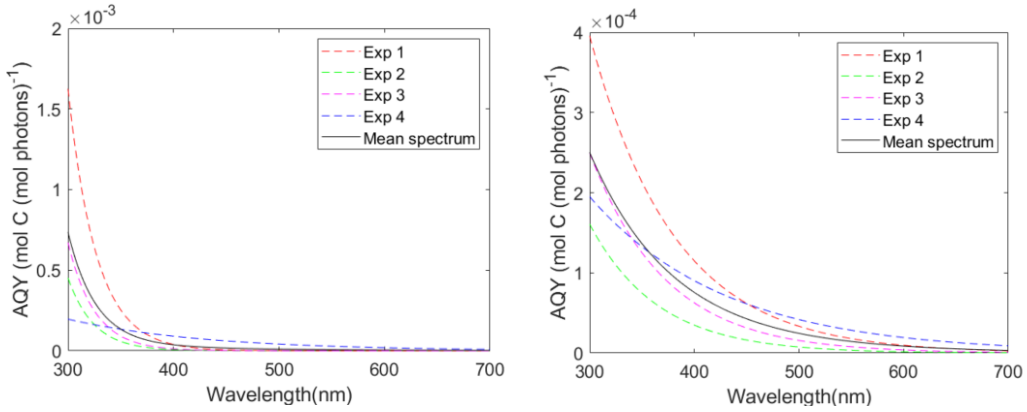

Figure S5. The AQY spectra of DOC photo-remineralization optimized using a starting value for c of 100 (left pane) and 0.01 (right pane). The AQY spectra in Fig. 4a in the original draft were optimized using a starting value of 1.0 as in Aarnos et al., (2018).

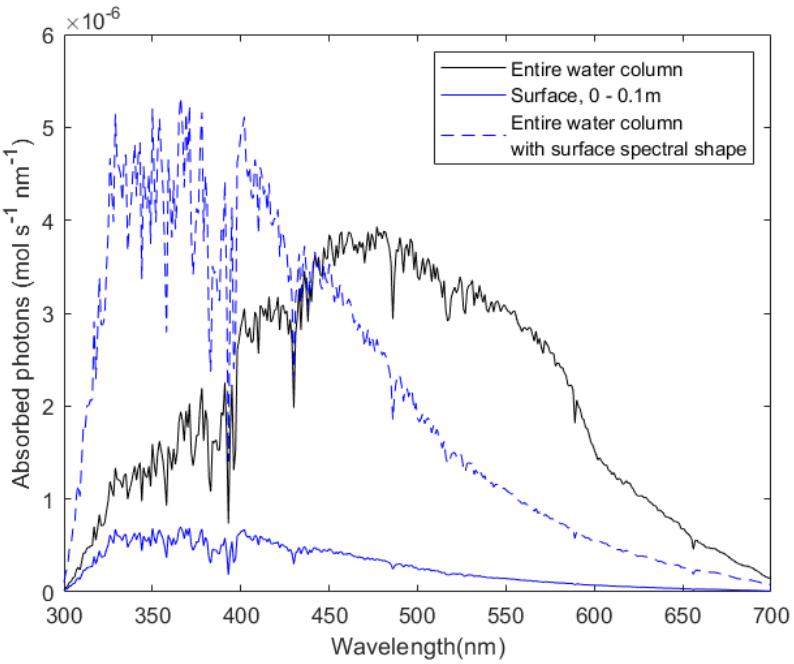

Figure S6. Spectra of photons absorbed by CDOM at the water surface (0 – 0.1m, solid blue line) and depth-integrated for the entire water column (solid black line) in our model for a 1-m^2 grid in the Southern Malacca Strait region with irradiance spectrum at noon of July 2019. The dashed blue line shows a hypothetical absorbed photon spectrum for the same total quantity of absorbed photons as for the black line, but with surface spectral shape (dashed blue line). The broadband AQY from our photodegradation experiments could only be

applied accurately to the whole water column if the spectrum of absorbed photons followed the dashed blue line, but in fact the absorbed photon spectrum is greatly shifted to longer wavelengths.

Table S1. Results from nitrite actinometry conducted following Jankowski et al., (1999). We measured the photo-production of salicylic acid in incubations in the Suntest solar simulator using experimental conditions as for our tDOC photodegradation experiments. The theoretically predicted photo-production of salicylic acid was calculated from the apparent quantum yield of salicylic acid production, the absorption spectrum of nitrite, and the irradiance spectrum of the test chamber as measured by the FLAME radiometer. The measured and predicted salicylic concentrations agree to within 6%, indicating that the irradiance spectrum measured by our radiometer can well represent the irradiance received inside the quartz cuvette we used for the photodegradation experiments.

Cut-off wavelength of the optical filter used	Predicted salicylic acid concentration (nM)	Measured salicylic acid concentration (nM)	% difference
295nm	163	168	-2.97
320nm	151	160	-5.63

Table S2. Variables in the photodegradation model.

Variable	Definition	Unit
a_{CDOM}	CDOM absorption coefficient	m^{-1}
a_W	Water absorption coefficient	m^{-1}
a_p	Particulate absorption coefficient	m^{-1}

bb_w	Water backscattering coefficient	m^{-1}
bb_p	Particulate backscattering coefficient	m^{-1}
K_d	Downwelling attenuation coefficient	m^{-1}
$E_{d,0+}$	Solar irradiance just above the sea surface	mol photons m^{-2} s^{-1}
$E_{d,0-}$	Solar irradiance just below the sea surface	mol photons m^{-2} s^{-1}
Ξ	Photons absorbed by CDOM	mol
λ	Wavelength	nm
θ	Solar zenith angle	degree
ϕ_{DOC}	Apparent quantum yield for photo-remineralization of DOC	Mol DOC (mol photons) $^{-1}$
ϕ_{CDOM}	Apparent quantum yield for photo-induced loss of volume-integrated CDOM absorption coefficient. For example ϕa_{350} is the apparent quantum yield for the photo-induced loss of volume-integrated CDOM absorption coefficient at 350nm.	L m^{-1} (mol photons)$^{-1}$

1668

1669

1670

1671

1672 Table S3. Changes in DOC and CDOM parameters during photodegradation experiments.

	DOC ($\mu mol\ L^{-1}$)	a_{350} (m^{-1})	$S_{275-295}$ (nm^{-1})	$SUVA_{254}$ ($L\ mg^{-1}\ m^{-1}$)
Exp 1 (Maludam River water, 416 hours)				
Initial	3250	167.4	0.011	5.41
End	850	5.9	0.021	1.23
%loss	74%	96%		
Exp 2 (diluted Maludam water, 462 hours)				
Initial	204	13.5	0.010	6.06
End	150	0.6	0.032	1.61
%loss	26%	96%		
Exp 3 (Singapore water during tDOC input, 500 hours)				
Initial	97	1.4	0.018	2.40
End	88	0.3	0.032	1.53
%loss	9%	79%		
Exp 4 (Maludam River water, 144hours, no-optical-filer treatment)				
Initial	3249	184.7	0.011	5.87

End	2268	85.9	0.014	4.52
%loss	30%	54%		

Table S4. The broadband Apparent Quantum Yield (AQY) for DOC photo-remineralization calculated for different time intervals from Exp 1 – 3. We did not observe a steady decrease in AQY over time. Only data before DOC concentration stopped to decrease were used to calculate AQY.

Exp No.	Time Interval (hour)	DOC loss (μmol) within the quartz cell	Absorbed photons (mol) Integrated over 290–700 nm	Broadband AQY (μmol C mol photons^{-1})
1 (Maludam Water)	0 – 72	15	0.15	100
	72 – 144	10	0.14	74
	144 – 216	8	0.12	64
	216 – 288	10	0.10	101
	288 – 258	12	0.08	153
	358 – 431	7	0.07	110
	0 – 431	63	0.66	95
2 (Maludam mixed with seawater)	0 – 51	0.33	0.014	25
	51 – 111	0.42	0.0087	48
	111 – 188	0.12	0.0069	16
	188 – 268	0.048	0.0044	11
	268 – 362	0.36	0.0028	128
	362 – 462	0.35	0.0019	178
	0 – 462	1.61	0.0383	42

3 (Singapore Strait)	0 – 24	0.078	0.00063	123
	24 – 70.5	0.075	0.00094	80
	70.5 – 119	0.017	0.00073	23
	119 – 170.5	0.074	0.00056	133
	0 – 170.5	0.24	0.0029	85

Table S5. Simulation results of tDOC remineralization by photodegradation in the Southern Malacca Strait using broadband AQY in the model, showing much larger tDOC loss compared to the results based on spectrally-resolved AQY (summarized in Table 2).

Conditions	Initial (μmol L^{-1})	Final (μmol L^{-1})	%loss
Clear-sky	108	45	58%
Cloud-corrected	108	63	42%

Table S6. Comparison of modelling results between using different starting values of coefficient *c* for optimizing AQY spectra.

	Initial DOC (μmol/L)	Final DOC (μmol/L)		
Starting value used		0.01	1.0	100
Southern Malacca Strait, cloud corrected	108	81	86	88
Talang Region, cloud corrected	181	173	174	176